Scientific Data

https://doi.org/10.1038/s41597-026-06823-1

Article in Press

Lattice-Boltzmann for Porous Media: 100M$^+$ GPU Hours

Received: 12 March 2025

Accepted: 4 February 2026

Cite this article as: Armstrong, R.T., Tavakkoli, O., Wang, Y. *et al.* Lattice-Boltzmann for Porous Media: 100M$^+$ GPU Hours. *Sci Data* (2026). https://doi.org/10.1038/s41597-026-06823-1

Ryan T. Armstrong, Omid Tavakkoli, Ying Da Wang, Zhe Li, Peyman Mostaghimi, Steffen Berg, Thomas Ramstad, Maja Rücker & James McClure

SCIENTIFIC DATA

Tracking no: SDATA-25-01248B

Lattice-Boltzmann for Porous Media: 100M GPU Hours

Authors: Ryan Armstrong (University of New South Wales), Omid Tavakkoli (University of New South Wales), Ying Da Wang (UNSW), Zhe Li (Australian National University), Peyman Mostaghimi (UNSW), Steffen Berg (Shell Global Solutions International), Thomas Ramstad (Equinor), Maja Ruecker (Eindhoven University of Technology), and James McClure (LBPM Project)

Abstract:
We present a comprehensive dataset of two-phase flow Lattice-Boltzmann simulations, generated using over 100 million GPU hours, covering a wide range of wetting conditions, capillary numbers, and porous geometries. While multiphase flow has traditionally been studied through laboratory experiments, the growing power of computational simulations provides a scalable and efficient alternative. Our simulations, validated against synchrotron beamline experiments, reveal key insights into the effects of wettability, ganglion dynamics, and flow behaviors that can be used to either substantiate current upscaling theories or develop new approaches. The dataset includes ~50 relative permeability curves and over 25,000 distinct fluid configurations. Acquiring equivalent data through experiments would be impractical using current techniques, and the computational resources required far exceed those typically available without direct access to high-performance facilities. This open-access dataset enables broad collaboration within the porous media research community and offers a valuable foundation for future studies on pore-scale transport, relative permeability prediction, and data-driven modeling approaches.

Datasets:

Repository Name	Dataset Title	Accession Number or DOI	URL to data record	Private reviewer access URL/code
Zenodo	LBPM Simulations	10.5281/zenodo.13836046	https://zenodo.org/records/13836047	

Lattice-Boltzmann for Porous Media: 100M$^+$ GPU Hours

Ryan T. Armstrong[1,*], Omid Tavakkoli[1], Ying Da Wang[2], Zhe Li[3], Peyman Mostaghimi[1,*], Steffen Berg[4], Thomas Ramstad[5], Maja Rücker[6,7], and James McClure[8]

[1]The University of New South Wales, School of Civil and Environmental Engineering, Sydney, 2552, Australia
[2]The University of New South Wales, School of Minerals and Energy Resources Engineering, Sydney, 2552, Australia
[3]The Australian National University, Research School of Physics, Canberra, 2601, Australia
[4]Shell Global Solutions International B.V., Amsterdam, The Netherlands
[5]Equinor ASA, Trondheim, Norway
[6]Eindhoven University of Technology, Mechanical Engineering, 5600 MB Eindhoven, The Netherlands
[7]Max Planck Institute for Polymer Research, 55128 Mainz, Germany
[8]Virginia Tech, Blacksburg, VA, USA
[*]corresponding author: Ryan T. Armstrong (ryan.armstrong@unsw.edu.au)

ABSTRACT

We present a comprehensive dataset of two-phase flow Lattice-Boltzmann simulations, generated using over 100 million GPU hours, covering a wide range of wetting conditions, capillary numbers, and porous geometries. While multiphase flow has traditionally been studied through laboratory experiments, the growing power of computational simulations provides a scalable and efficient alternative. Our simulations, validated against synchrotron beamline experiments, reveal key insights into the effects of wettability, ganglion dynamics, and flow behaviors that can be used to either substantiate current upscaling theories or develop new approaches. The dataset includes 50 relative permeability curves and over 25,000 distinct fluid configurations. Acquiring equivalent data through experiments would be impractical using current techniques, and the computational resources required far exceed those typically available without direct access to high-performance facilities. This open-access dataset enables broad collaboration within the porous media research community and offers a valuable foundation for future studies on pore-scale transport, relative permeability prediction, and data-driven modeling approaches.

Background & Summary

For applications ranging from underground hydrogen storage[18] and carbon dioxide sequestration[17] to processes in gas diffusion layers in electrolysis and fuel cells[14–16], the effective transport of immiscible fluid phases in porous media, often parameterized as relative permeability, is crucial. Traditionally determined from laboratory flow experiments, numerical simulations have become an important tool to determine relative permeability[43,45]. In particular, recent advances in computational power and fundamental techniques now allow for a detailed exploration of a significant parameter space at the pore scale that would not be feasible/practical to collect experimentally[44]. In the following, we will explain the utility of the shared simulation data and the various challenges associated with conducting such simulations.

In general, pore-scale simulation techniques vary in rigor, detail, scale, and computational cost, ranging from direct pore-scale simulations[19] to mechanistic models, such as pore network modeling[24]. Direct pore-scale simulation methods differ in their treatment of the liquid-liquid interface, from sharp interface methods like level set[26] to diffuse interface methods such as phase field methods[20,23], smooth particle hydrodynamics[25], and Lattice Boltzmann method (LBM) [19]. LBM is particularly popular for its balance of rigor, lower computational cost, and ease of parallelization[9,21]. In particular, for the simulation data shared in this paper, the Lattice Boltzmann for Porous Media (LBPM) software was used; see `https://github.com/OPM`.

Despite the efficiency of the LPM, simulations still require substantial time steps, which depend on the domain size, fluid parameters, flow regime, and convergence criteria used. As demonstrated by[9], for steady-state simulations (on the order of 1000^3 voxels), approximately 250,000 to 350,000 time steps are required for a single relative permeability point. In terms of real-time, achieving accurate results for a single saturation point can take approximately three hours using 80 GPUs[5,9]. Decreasing the capillary number or reaching a saturation end point, particularly for mixed-wet or oil-wet conditions, can increase the number of time steps by a factor of 10^9. Strategies to reduce computational costs without compromising rigor include morphological initialization and deep learning-assisted time stepping and initialization[27–29].

Accurate simulations require detailed pore-scale models, including variations in complex geometry and / or wettability[30]. Mixed-wet systems[32] further complicate simulations, especially in structures with a large surface area and the potential for numerous small droplets. LBPM uses sophisticated algorithms to simulate fluid interactions within the porous medium, including small droplet formation and movement, providing detailed fluid flow analysis and improving the interpretation of simulations of relative permeability[5]. The subphase tracking algorithm offers direct insight into the phase morphological parameters per time step, identifying complications or physical mechanisms such as ganglion dynamics[31].

Upscaling from the pore scale to the Darcy scale remains a fundamental challenge. Although linking pore-scale fluid structures to continuum-scale hydraulic conductivities is widely accepted as a general approach, the specifics vary widely[4,6,33–36]. Capturing pore-scale fluctuations[46], such as fluid morphological variations, is crucial for theoretical development. Balancing computational efficiency with the analysis of pore-scale entities is another challenge[44]. In particular, the morphological measures of pore-scale entities, such as interfaces, are critical for various up-scaling theories. Moreover, geometric measures, conserved quantities, and thermodynamic measures as listed in Table 1 are not easily accessible from pore-scale experiments and/or other simulation tools, which require subsequent image processing to obtain. Practical implementation and integration of pore-to-core scale modeling remain challenging, necessitating the need for quality data that provide simultaneous measures at both length scales, such as pore-scale phase morphology and resulting relative permeability.

Experimentally, relative permeability is collected using the steady-state or unsteady-state method[8]. In the case of rocks, the sample is aged for 2-8 weeks to establish a wetting condition[47]. The steady-state method is time-consuming, as it involves the injection of many pore volumes for each fractional flow[8]. An entire steady-state relative permeability curve can take 1-2 weeks to collect. The unsteady-state method can be considerably faster, yet it does not provide the entire relative permeability curve for all saturations. A conservative time estimate for a steady-state relative permeability curve for a single wetting state is approximately 1.5 months. In comparison, with direct simulation and high-performance computing, a steady-state relative permeability curve for a single wetting state requires an order of magnitude less time. This, of course, depends on the exact computational domain, fluid parameters, and available computing resource. Another advantage of direct simulation is that geometrical information at the pore scale is readily available, which can be determined per computational time step[44]. Traditional experimental methods do not provide information on the pore-scale geometry of fluids[8]. Such experimental studies require millimeter-diameter core plugs that can be imaged with X-ray computed microtomography at micrometer resolution[49]. The measurement of geometrical features then requires extensive image processing and analysis[48], which makes it impractical to collect data in a large parameter space.

Herein, our aim is to provide a collection of pore-scale simulations that would not be experimentally feasible/practical to conduct and would be computationally restrictive to create. The shared data, based on more than 100M+ GPU hours, is an uncommon resource, providing valuable information for the broader community. In general, the simulation data provided are available for the porous media community to collaborate on complex multiscale and multidisciplinary questions, including multiphase flow upscaling, deep learning applications, identification of computational reducibility, and establishing industry workflows for digital rock technology.

Methods

The LBPM simulation tool offers several advanced capabilities to address the challenges of relative permeability simulations[9]. It incorporates the morphological Lattice Boltzmann Method (LBM), which significantly reduces computational costs by decreasing the number of required time steps. This approach allows for more efficient simulations while maintaining accuracy in modeling fluid flow through porous media. The tool is designed to handle complex geometries and mixed-wet systems, accurately capturing high-surface-area structures and small droplets. LBPM also facilitates the upscaling process from the pore scale to the Darcy scale, ensuring that pore structures are effectively linked to continuum-scale hydraulic conductivities. In addition, the simulation tool accounts for fluctuations in wettability and fluid distribution, enhancing the reliability of the results. It also balances computational efficiency with model accuracy, providing robust simulations without excessive computational demands. The tool's sensitivity analysis and data normalization capabilities ensure that the parameters are accurately reflected in the simulations.

Lattice Boltzmann Method

Fluid flow simulations were performed using a parallel implementation of the color gradient Lattice Boltzmann method[9]. The code is available as part of the Open Porous Media Project, see `https://github.com/OPM` for further details. The color gradient Lattice-Boltzmann method will not be explained in detail here since a large body of work already exists that explains the theory and implementation. Instead, we will focus on the unique analysis capabilities of LBPM that provide a framework for testing and developing multiphase flow theories and their application to measure relative permeability under variable wetting conditions. This includes standard protocols aligned with common core analysis techniques and *in situ* analysis capabilities to perform upscaling based on the microscale simulation state. The averaging framework can be used to determine a variety of

averages in the phases, interfaces, and the common curve[11–13]. For example, macroscopic flow velocities can be determined for each phase by computing the total momentum and dividing it by the total mass. Additional quantities can also be computed, including average phase pressures, average velocities for the interface and common curve, average mean curvature of the interface between fluids, and other measures defined from multiscale averaging theory[54].

Wettability

In the LBPM framework, a wetting map is used to characterize the spatial distribution of the wettability. This wetting map assigns a distinct label to each solid voxel, with each label corresponding to a specific wetting affinity. The affinity value (ϕ_s) serves as a pseudo-phase field that represents the wettability of each voxel within the porous medium. The correlation between ϕ_s and the equilibrium contact angle (θ_{eq}) is expressed by the following equation:

$$\cos\theta_{eq} = \phi_s \tag{1}$$

This relationship indicates that ϕ_s directly influences the equilibrium contact angle, thereby governing the surface wettability at a microscopic scale. The affinity value ranges from -1.0 (strongly oil wet) to 1.0 (strongly water wet).

Bulk volumetric wettability is characterized as the summation of the cosine of the contact angles for each solid/fluid/fluid combination, determined as

$$W = \sum(\gamma_{io} - \gamma_{iw})/\gamma_{wn}\phi_i \tag{2}$$

where ϕ_i is the solid voxel fractions of solid i, γ_{io} is interfacial tension between solid i and the oil phase, and γ_{iw} is interfacial tension between solid i and the water phase. This metric provides a wetting index from strongly water wet ($W = 1.0$) to strongly oil wet ($W = -1.0$). It should be noted that W is a volumetric metric, which may deviate from the wetting conditions along the mineral surfaces. However, for the simulations provided, this volumetric metric was used as a simple way to characterize the wetting state.

More recently, LBPM now has a more direct measure of wetting, which is the integral of the surface energy

$$\gamma_s A_s = \int_{\Gamma_s} \gamma \, dS \,, \tag{3}$$

where Γ_s is the solid grain boundary. The quantity γ_s is therefore the average fluid-solid surface energy of the system, accounting for both the fluid configuration and the relevant fluid-solid interactions. This is tracked in both the *basic* and *subphase* analysis modules and corresponds to the thermodynamically correct surface energy.

Capillary Number

The capillary number (Ca) is a dimensionless parameter that characterizes the balance between capillary and viscous forces in a fluid flow. The conventional definition of capillary number becomes ambiguous in the context of multiphase flow, since the viscosities and velocities of constituent fluids can vary independently. Within the LBPM framework, a comprehensive formula is employed to determine the total capillary number, which accounts for interactions between multiple fluid components. The total capillary number is defined as

$$Ca = \frac{\varepsilon_a \mu_a |\mathbf{u_a}| + \varepsilon_b \mu_b |\mathbf{u_b}|}{\sigma}, \tag{4}$$

where ε represents the volume fraction of the fluids, μ is the dynamic viscosity of fluids, $\mathbf{u}$ and σ denote average momentum flux rate and interfacial tension between fluids, respectively. This formulation ensures a representative value for the capillary number, even when the flow rate within one of the fluids is effectively zero. For LBPM, Ca is an outcome of the parameters assigned in the input file, i.e., body force, viscosity, and interfacial tension.

Sub-phase *in situ* Analysis

The subphase analysis involves a detailed examination of the geometric, conserved, and thermodynamic quantities during simulation. This analysis is crucial to understanding the behavior and characteristics of fluid flow. The primary objective of the subphase analysis is to capture the spatial and temporal evolution of each fluid phase and their interactions. The process begins with the identification of fluid regions, defined as volumetric areas occupied by either the wetting phase (phase indicator $\phi > 0$) or the nonwetting phase ($\phi < 0$), along with fluid interfaces characterized by significant composition gradients ($|\nabla\phi| \geq \varepsilon$). Each region is further subdivided into connected and disconnected subentities for detailed analysis, which encompasses geometric, conserved, and thermodynamic quantities. Table 2 provides detailed information on the main quantities measured. For a complete list of measures, the reader is referred to *LBPM documentation* (https://lbpm-sim.org) or Tables 3 and 4.

Relative Permeability Protocols

Simulation protocols have been developed to model unsteady state and steady state flows. Both protocols closely mirror traditional laboratory relative permeability experiments[8].

- The unsteady-state protocol is designed to replicate the dynamic process of one fluid displacing another. In these simulations, the volume fraction of each fluid changes over time as a result of continuous fluid injection. To simulate an unsteady-state core flood, the flux boundary condition was used, which involves applying a constant volumetric flow rate at the inlet.
- For steady-state simulations, periodic boundary conditions are used to maintain constant saturation and avoid boundary effects. The achievement of a steady state is evaluated by monitoring Ca over a defined time-step interval. The steady state is confirmed when the change in Ca falls below a user-specified tolerance, ensuring stable flow behavior. At this point, the fluid saturation is updated for simulation of the next fractional flow.

The initial fluid configurations can be obtained from segmented micro-computed tomography (micro-CT) images of multiphase flow at a given fractional flow. These labeled images distinguish between various phases, including solid, nonwetting fluid, and wetting fluid. In cases where multiphase micro-CT images are not available, morphological operations can be used to set the initial fluid configurations. The primary drainage process is often used to simulate the initial invasion of the nonwetting phase into a porous medium saturated with the wetting phase. The morphological drainage operation utilizes the distance transform of the pore space to define the largest sphere that can fit within the pores and then gradually reduces the radius to simulate fluid invasion. This process is also used for mixed-wet conditions where, following the primary drainage, solid voxels near the nonwetting fluid are re-labeled to simulate an aging process[9]. This aging process alters the wetting state of solid surfaces, making them more favorable to the nonwetting fluid. In addition, the shell aggregation protocol is employed to incrementally adjust the fluid configuration to achieve different saturations[27]. This protocol involves slightly moving the boundary of fluid phases and then allowing the system to relax the phase configuration towards minimal-energy states using LBM simulation.

Relative permeability is a fundamental parameter for the characterization of multiphase flow in porous media[41]. Relative permeability quantifies the effective permeability of each fluid in the presence of other fluids, normalized by the absolute permeability of the porous domain. The effective permeability (k) for each fluid is determined based on the velocity of the fluid, the dynamic viscosity, and the driving forces, including the pressure gradient (∇p_i) and the external body force (g), as stated in the multiphase extension of Darcy's law:

$$u_i = \frac{k_i}{\mu_i}(\rho g - \nabla p_i). \tag{5}$$

The average flow velocity is computed by:

$$\langle \mathbf{u} \rangle_a = \frac{\mathbf{P}_a}{M_a}, \tag{6}$$

where $\mathbf{P}_a$ and M_a are the total momentum and the total mass, respectively, for the fluid a.

Simulation domains

The simulation domains include four different porous structures based on X-ray computed microtomography images. Each domain differs in terms of image resolution, pore sizes, rock type, domain size, and applied wetting conditions. An important condition for the LBPM simulation is image resolution versus average pore size. With LBPM, the thickness of the interface is approximately 3 voxel lengths. To capture the physics of capillary-dominated flow, the majority of pores need to be resolved by more than 3 voxels.

Bentheimer sandstone I

Bentheimer sandstone ($\phi = 24\%$, $K = 1.3D$) was imaged with X-ray computed microtomography and segmented using Avizo software[50]. The image resolution was 7.0 μm. The domain size was $600 \times 594 \times 1312$ voxels. The operation of a morphological drainage in the Bentheimer domain shows that the entry pressure corresponds to a throat radius of 2.5 voxels, which is equal to the thickness of the interface in LBPM. In addition, the throats are extremely homogeneous and relatively small compared to the pore bodies. As shown in the results below, the image resolution affected the simulation results, which could have been removed from the uploaded data, but is provided here as an instructional example of what would happen due to poor image resolution, which is overlooked in some published works.

For the assignment of wettability, oil was injected on the basis of a morphological approach to achieve irreducible water saturation. Parts of the grain surface that touch oil get their own wetting condition while corners remain wet with water. The bulk wetting conditions were quantified in terms of W.

North Sea sandstone

The North Sea sandstone domain ($\phi = 23\%$, $K = 640mD$) was generated by X-ray microcomputed tomography (micro-CT) in combination with Electron Microscopy Energy Dispersive Spectroscopy (SEM-EDS)[52]. The SEM-EDS data was digitally registered with the 3D micro-CT data at 2.0 μm resolution. The domain size was $1000 \times 1002 \times 750$ voxels. The pore size was on the order of 20 μm, which means that it was well resolved in terms of the thickness of the interface with LBPM.

3D mineral segmentation was performed by distinguishing the X-ray intensity range of each mineral provided by registering the 2D to 3D data sets. For simplification, QEMSCAN minerals were clustered into three groups. The first group is called quartz, which includes quartz, plagioclase and feldspar, which was 74% of the solid grains. The second group was called clay, which includes; kaolinite, illite and muscovite. The clay group made up 19% of the solid voxels. The third group was called carbonate, which includes all other minerals. This group consisted of 6.3% of the solid voxels.

We tested four different ways to assign wettability distributions, all of which have a basis in special core analysis[8].

1. Homogeneous: the same condition over the entire grain surface.
2. Mixed: oil is injected on the basis of a morphological approach to achieve irreducible water saturation. Parts of the grain surface that touch oil get their own wetting condition while corners remain water wet.
3. Spotted: each mineral type gets a different wettability.
4. Hybrid: a combination of 2 and 3.

The bulk wetting conditions were quantified in terms of W. Each simulation is also indexed in terms of its type of wettability assignment.

Robuglass

A sintered glass sample called Robuglas ($\phi = 33\%$, $K = 22D$) was imaged with X-ray computed microtomography at 4.2 μm and segmented using the Avizo software[51]. The domain size was $990 \times 990 \times 1188$ voxels. The average pore diameter for the Robuglas sample was around 50 micrometers. Therefore, a significant fraction of the pore space was resolved by more than 3 voxels.

The domain was simulated with a single water-wet condition, $W = 1$, over a wide range of different Ca.

Bentheimer Sandstone II

A second Bentheimer sandstone ($\phi = 24\%$, $K = 1.9D$) was imaged with X-ray computed microtomography at 1.7 μm and segmented using the Avizo software[53]. The domain size was $900 \times 900 \times 1600$ voxels. Based on morphological drainage results, at $S_w = 0.15$ the diameter of the minimum occupied pore throat was 10 voxels. This provided a throat radius greater than the width of the interface.

For the assignment of wettability, oil was injected on the basis of a morphological approach to achieve irreducible water saturation. Parts of the grain surface that touch oil get their own wetting condition while corners remain wet with water. The bulk wetting conditions were quantified in terms of W.

Data Records

Each domain was simulated as specified in Table 1. The simulations included a wide range of different wetting conditions, W, capillary numbers, and boundary conditions. The basic analysis routine for the LBPM color model logs a time series of averaged information into a space-delimited CSV file. These measures include water saturation (sw), effective permeability of fluid w (krw), effective permeability of fluid n (krn), speed of fluid w (vn), speed of fluid n (vn), magnitude of effective force ($force$), average pressure for fluid w (pw), average pressure for fluid n (pn), total solid wetting energy (wet). In addition, the subphase analysis routine for the LBPM color model logs a more detailed time series of averaged information to the space-delimited CSV file. These measures are listed in Tables 3 and 4.

All CSV files are provided at Zenodo[55]. Each simulation study is organized into a directory based on the porous domain used for the simulation. Within a given directory, each simulated case is organized within its own subdirectory. The subdirectory names provide a general guide to the simulation conditions used, while `input.db` provides the specific input simulation conditions. Data analysis can be conducted from the R scripts provided within the main directory. These scripts read the CSV files from each simulation case and provide typical data analysis measures, such as Capillary number, effective permeability, Minkowski measures, or ganglion flux. All R scripts have been tested, and the output figures are provided in the main directory.

The 3D domains are available through the Digital Rocks Portal https://www.digitalrocksportal.org as follows.

- Bentheimer I[50]

- North Sea[52]
- Robuglass[51]
- Bentheimer II[53]

Storage of 3D fluid distributions is massive and not saved. The relevant physics and a complete set of morphological measures are captured in the provided CSV files. 3D images can be recreated by running LBPM (https://github.com/OPM/LBPM) with the provided image domains and input files.

Technical Validation

In the following section, a brief overview of the observed trends will be presented to assess the technical quality of the simulations and provide insight into the quality of the results to help guide the use of the data and/or the design of future simulations.

Bentheimer Sandstone I

Figure 1 illustrates an example of *Ca* convergence, highlighting that a significant number of time steps are necessary to reach a steady state, especially at lower *Ca*, where convergence requires even more steps. The data presented are for water saturation at 30% and wetting condition $\phi_s = -0.5$. All Bentheimer Sandstone I simulations have similar behavior in addition to all simulations in the other domains, with the specific conditions dictating the number of time steps required for convergence. Please note that the convergence data are available in the shared CSV files for all simulations and domains.

The effective permeability curves for all simulations on Bentheimer sandstone are presented in Figure 2. We observe a general reduction in the relative permeability of the water phase and an increase in the relative permeability of the oil phase for any given saturation as the medium becomes more water wet. This trend is likely explained by the early snap-off of NWP in the more water-wet cases as a result of limited resolution of the throats. This results in rather flat relative permeability curves, with essentially all pores quite narrow in terms of image resolution.

Residual oil saturation versus wettability is shown in Figure 3. The results are aligned with various experimental works in which residual oil saturation decreases under more oil-wet conditions. For water-wet simulations, the oil phase is trapped by snap-off, resulting in a trapped phase that no longer flows at a low *Ca*. For intermediate-wet to oil-wet conditions, the oil phase drains through a thin-film flow. The hydraulic conductivity of these films is relatively low and therefore drainage occurs on a long time scale. This becomes an issue in terms of computational time since residual oil saturation is reached only once a sufficient number of pore volumes have been pumped through the domain. Up to 18 million time steps were required for the simulations to reach residual oil saturation under oil-wet to mixed-wet conditions. The residual saturation obtained with fewer time steps does not follow the trend provided in Figure 3. This is an important issue when simulating end-point relative permeability using LBPM and other pore-scale simulation methods.

North Sea Sandstone

The effective permeability curves for all North Sea sandstone simulations are shown in Figure 2. The observed shift in the relative permeability with wettability is well aligned with previously published experimental results. The North Sea sandstone domain was well resolved in comparison to the Bentheimer sample. However, close inspection of the S_{or} end-points does not align well with that observed for the Bentheimer sample. For the North Sea sandstone, nearly the same end point was obtained for all simulations, due to the applied simulation protocol. The LBPM Steady-State simulation protocol was used, which does not use a final so-called 'pump flood' of pure water to establish residual saturation. Such protocols are commonly used in experiments to obtain residual saturation after performing the steady-state core flooding method[8].

LBPM simulations with the subphase analysis provide a means of exploring the evolution of fluid morphological parameters. The Euler characteristic for the connected NWP for each wetting condition is shown in Figure 5 while the Euler characteristic for the connected WP is shown in Figure 6. As the Euler characteristic of the connected phase approaches zero, the function develops a plateau region that corresponds to either increased disconnected phase flow at high *Ca* or fluid trapping at lower *Ca* flows. For intermediate wet conditions, both the WP and the NWP maintain mutually high connectivity, corresponding to the existence of minimal surfaces as observed in the cores treated with crude oil[42]. Additionally, we observe that the general evolution of the Euler characteristic for either phase follows a consistent pattern that is well correlated with the bulk wetting index, W.

Robuglass

The relative permeability curves for all simulations are shown in Figure 7. The solid lines correspond only to the relative permeability of the connected phase, i.e., low *Ca* flow. The open symbols correspond to the relative permeabilities as *Ca*

increases. The general trend with *Ca* is as expected from similar experimental studies. The subphase data provide a means to measure ganglion flux in addition to other morphological measures. A unique capability is the ganglion tracking algorithm, which allows the mapping of ganglion trajectories in time and space. Figure 8, provides an example of this capability in which the projection of ganglion trajectories is mapped in the Z-X plane. Future works could use the provided data to account for the disconnected phase flow using subphase modeling, in which the transport of connected and disconnected phase flows are modeled separately with a mass transfer coefficient between the two subphases[7]. The phase morphological data for these simulations were validated with dynamic sychrotron-based X-ray computed microtomography experiments, as reported by[5].

Bentheimer Sandstone II

The relative permeability curves for all simulations are shown in Figure 9. The expected shift in the relative permeability curves with wettability is observed, as also observed with the North Sea sandstone. An important observation is that a misleading trend in wettability is observed when image resolution is not sufficient (see Figure 2. Bentheimer Sandstone II results also provided typical 'smiley face' trends with S_{or} versus resolution where a minimum in S_{or} is observed under intermediate wet conditions. This data is not shown since it has been published elsewhere; see[9], yet it is provided in the shared data files. In addition, the fractional flow versus pressure drop results are provided in Figure 10. The observed behavior is in good alignment with the behavior expected from core flooding studies[8].

Figure 11 demonstrates the divergent behavior of the Euler characteristic for different wetting conditions. Under oil-wet conditions, the NWP connectivity becomes a maximum at intermediate wet saturations as the NWP coats the grains but has yet to completely fill the pore space. For water-wet conditions, the NWP fills the pore space but maintains a nearly constant connectivity until the pores are mostly filled with NWP, in which case the NWP connectivity approaches that of the domain. All simulations approach the domain connectivity at complete NWP saturation, yet the trajectory taken is highly dependent on the wetting condition.

Usage Notes

Full details on LBPM are provided at (https://lbpm-sim.org). The subphase analysis measures geometric variants, conserved quantities, and thermodynamic quantities. Geometric measures include volume, surface area, integral of mean curvature, and Euler characteristic. The conserved quantities include the total mass within a region, the total momentum within the region, and the total kinetic energy within the region. Thermodynamic quantities include pressure, solid wetting energy, and viscous dissipation. The definition of each parameter found in the CSV files of the subphase analysis is provided in Tables 3 and 4. These simulation results have been used in other relevant publications, as listed in Table 1.

In addition to the simulation data, R scripts are provided to generate basic plots, such as phase morphologies versus saturation and relative permeability curves that include various other measures. These scripts provide a basic overview and an introduction to working with the data files. The simulation input files are called 'input.db', which provide the specific parameters used for each simulation, including the simulation protocol that was used, convergence criteria, phase viscosity, body force, and interfacial tension. The subphase analysis is provided per time step as defined in the input file. 3D images of fluid distributions per time step are not provided because of memory limitations. The subphase analysis provides all of the typical morphological measures taken from the 3D fluid distribution images and dynamic properties relevant for upscaling theories and other developments, as outlined in the Background and Summary section.

Data availability

All simulation files are available at `https://zenodo.org/records/13836047`.

Code availability

LBPM is available through the Open Porous Media Project - `https://github.com/OPM`. The software is published under GPL-3.0 license (GNU General Public License).

References

Acknowledgements

R. T. A. acknowledges Australian Research Council Future Fellowship (FT210100165) and Discovery (DP210102689). This research used resources from the Oak Ridge Leadership Computing Facility, which is a DOE Office of Science User Facility supported by the DE-AC05-00OR22725 contract.

Author contributions statement

R. T. A. contributed digital domains for wettability studies, conducted investigations on wettability and Capillary number effects, provided funding acquisition for wettability studies, and wrote the original draft. O. T. provided formal analysis of simulation convergence, data curation, and visualization of results. Y. D. W. contributed to the development of multi-mineral models and related wettability studies. Z. L. developed the LBPM wetting models and related software capabilities. P. M. contributed to the wettability studies and related funding acquisition. S. B. contributed to the conceptualization and investigation of simulation protocols. T. R. contributed to the conceptualization and investigation of simulation protocols. M.R. contributed to the processing of the experimental data. J. M. developed the LBPM software, conducted the formal analysis, investigation, conceptualization, and acquisition of computational resources.

All authors contributed to the review and editing of the article.

Competing interests

The authors declare that they have no competing interests.

Figures & Tables

Rock Type	Resolution	Domain Size	Protocol	Mode	Published Works
Bentheimer I	7.0 μm	$600 \times 594 \times 1312$	SS	NA	None
North Sea	2.3 μm	$1000 \times 1002 \times 750$	SS	NA	[1,2]
Robuglass	X.X μm	$990 \times 990 \times 1188$	SS	NA	[4–6]
Bentheimer II	1.7 μm	$900 \times 900 \times 1600$	USS	Imbibition	[9,10]

Table 1. Rock types evaluated, simulations conducted, and other published works that have thus far used the shared simulation data.

Quantities	**Symbol**	**Definition**	**Description**
Sub-entities	Ω_{wc}	-	Connected part of phase w
	Ω_{wd}	-	Disconnected part of phase w
	Ω_{nc}	-	Connected part of phase n
	Ω_{nd}	-	Disconnected part of phase n
	Ω_{ic}	-	Connected part of the interface region
	Ω_{id}	-	Disconnected part of interface region
Geometric	V_k	$V_k = \int_{\Omega_k} dV$	Total volume for region k
	A_k	$A_k = \int_{\Gamma_k} dS$	Total surface area for region k
	H_k	$H_k = \int_{\Gamma_k} \frac{1}{2}(\kappa_1 + \kappa_2) dS$	Integral mean curvature for region k
	χ_k	$\chi_k = \frac{1}{4\pi} \int_{\Gamma_k} \kappa_1 \kappa_2 dS$	Euler characteristic for region k
Conserved	M_k	$M_k = \int_{\Omega_k} \rho dV$	Total mass for region k
	$\mathbf{P}_k$	$\mathbf{P}_k = \int_{\Omega_k} \rho \mathbf{u} dV$	Total momentum for region k
	K_k	$K_k = \frac{1}{2} \int_{\Omega_k} \rho \mathbf{u} \cdot \mathbf{u} dV$	Total kinetic energy for region k
Thermodynamic	p_k	$p_k = \frac{1}{V_k} \int_{\Omega_k} p dV$	Average pressure for region k
	γ_s	$\gamma_s = \int_{\Gamma_s} \gamma dS$	Solid wetting energy
	Φ_k	$\Phi_k = \int_{\Omega_k} \varepsilon : \nabla \mathbf{u} dV$	Viscous dissipation

Table 2. Sub-entities and measured quantities within sub-phase analysis.

References

1. Al-Zubaidi, Fatimah and Mostaghimi, Peyman and Niu, Yufu and Armstrong, Ryan T and Mohammadi, Gelareh and McClure, James E and Berg, Steffen. Effective permeability of an immiscible fluid in porous media determined from its geometric state. Physical Review Fluids (2023).

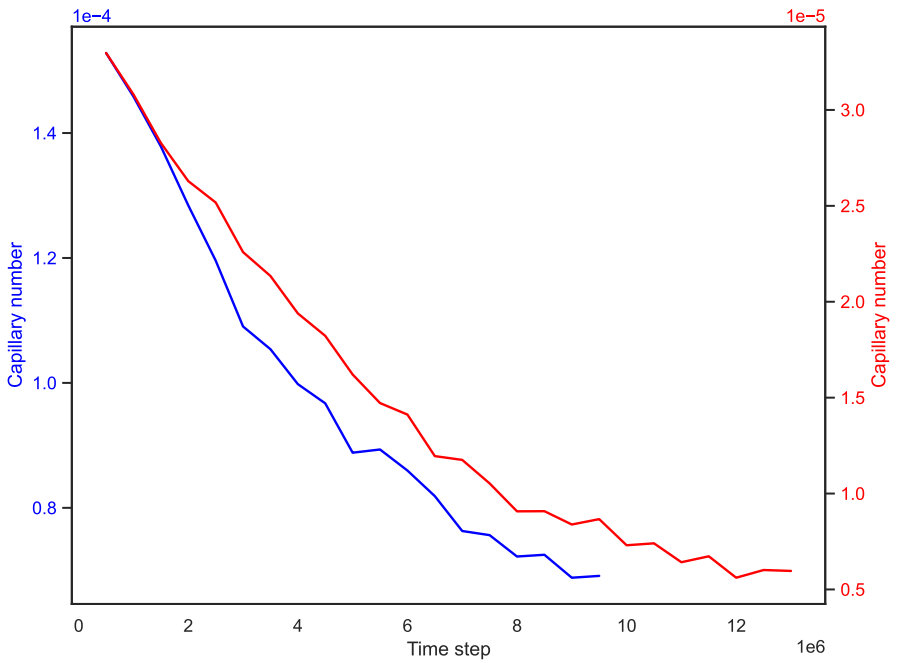

Figure 1. Capillary number convergence for Bentheimer I at $S_w = 0.30$ for two different body forces. For the red curve the target was $Ca = 1e^{-5}$ while for the blue curve and target was $Ca = 1e^{-4}$.

2. Alzubaidi, Fatimah and McClure, James E and Pedersen, Hå. The impact of wettability on the co-moving velocity of two-fluid flow in porous media. arXiv preprint arXiv:2309.00362 (2023).
3. Khorsandi, Saeid and Li, Liwei and Johns, Russell T. Equation of state for relative permeability, including hysteresis and wettability alteration. SPE Journal (2017).
4. Picchi, D and Battiato, I. Relative permeability scaling from pore-scale flow regimes. Water Resources Research (2019).
5. Armstrong, Ryan T and McClure, James E and Berrill, Mark A and Rü. Beyond Darcy's law: The role of phase topology and ganglion dynamics for two-fluid flow. Physical Review E (2016).
6. Purswani, Prakash and Tawfik, Miral S and Karpyn, Zuleima T and Johns, Russell T. On the development of a relative permeability equation of state. Computational Geosciences (2020).
7. Khayrat, Karim and Jenny, Patrick. Subphase approach to model hysteretic two-phase flow in porous media. Transport in porous media (2016).
8. McPhee, Colin and Reed, Jules and Zubizarreta, Izaskun. Core analysis: a best practice guide. (2015).
9. McClure, James E and Li, Zhe and Berrill, Mark and Ramstad, Thomas. The LBPM software package for simulating multiphase flow on digital images of porous rocks. Computational Geosciences (2021).
10. Armstrong, Ryan T and Sun, Chenhao and Mostaghimi, Peyman and Berg, Steffen and Rü. Multiscale characterization of wettability in porous media. Transport in Porous Media (2021).
11. McClure, JE and Adalsteinsson, D and Pan, C and Gray, WG and Miller, CT. Approximation of interfacial properties in multiphase porous medium systems. Advances in water resources (2007).
12. Mcclure, James E and Berrill, MA and Gray, WG and Miller, CT. Tracking interface and common curve dynamics for two-fluid flow in porous media. Journal of Fluid Mechanics (2016).
13. McClure, JE and Pan, C and Adalsteinsson, D and Gray, WG and Miller, CT. Estimating interfacial areas resulting from lattice Boltzmann simulation of two-fluid-phase flow in a porous medium. (2004).
14. Mularcyk, A. and Lin, Q. and Blunt, M. J. and Lamibrac, A. and Marone, F. and Schmidt, T. J. and Bü. Droplet and percolation network interactions in a fuel cell gas diffusion layer. J. Electrochem Soc. (2020).
15. Eller, J. and Rosen, T. and Marone, F. and Stampanoni, M. and Wokaun, A. and Bü. Progress in In situ X-ray tomographic microscopy of liquid water in gas diffusion layers of PEFC. J. Electrochem Soc. (2011).

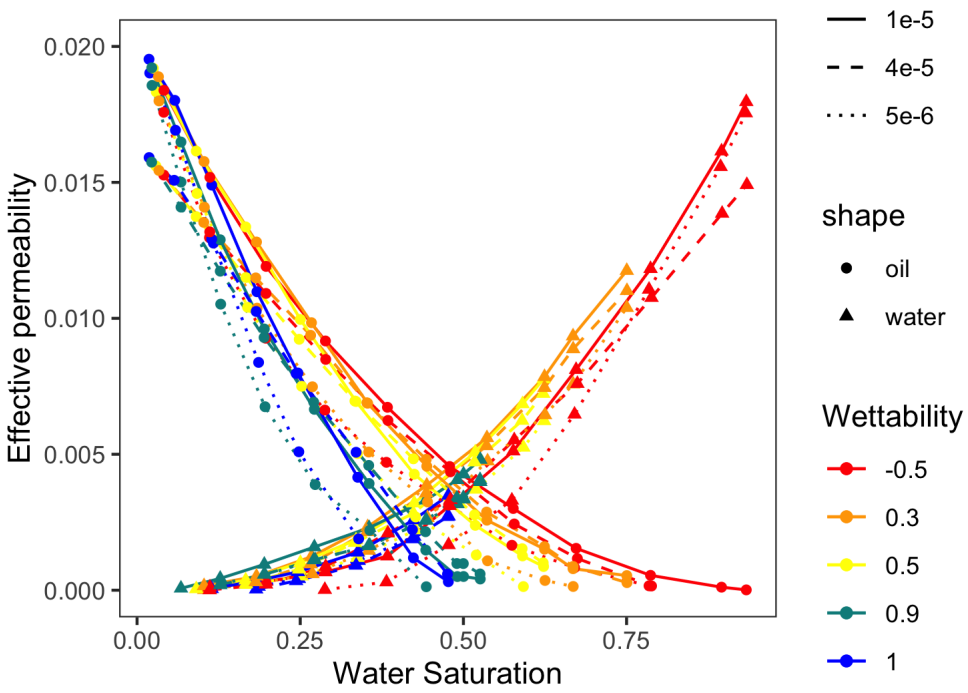

Figure 2. Relative permeability data for Bentheimer sandstone. The data ranges over various capillary numbers and wettabilities from water wet to oil wet rock.

16. Arlt, T. and Klages, M. and Messerschmidt, M. and Scholta, J. and Manke, I.. Influence of artificially aged gas diffusion layers on the water management of polymer electrolyte membrane fuel cells analyzed with in-operando synchrotron imaging. Energy (2017).

17. Zhang, Y. and Nishizawa, O. and Kiyama, T. and Chiyonobu, S. and Xue, Z.. Flow behaviour of supercritical CO2 and brine in Berea sandstone during drainage and imbibition revealed by medical X-ray CT images. Geophys J. Int. (2014).

18. Higgs, S. and Da Wang. Comparative analysis of hydrogen, methane and nitrogen relative permeability: Implications for Underground Hydrogen Storage. Journal of Energy Storage (2023).

19. Meakin, P. and Tartakowsky, A. M.. Modeling and simulation of pore-scale multiphase fluid flow and reactive transport in fractured and porous media. Journal of Energy Storage (2009).

20. Alpak, F. O. and Zacharoudiou, I. and Berg, S. and Dietderich, J. and Saxena, N.. Direct simulation of pore-scale two-phase visco-capillary flow on large digital rock images using a phase-field lattice Boltzmann method on general-purpose graphics processing units. Computational Geosciences (2019).

21. Liu, Haihu and Kang, Qinjun and Leonardi, Christopher R and Schmieschek, Sebastian and Narvá. Multiphase lattice Boltzmann simulations for porous media applications: A review. Computational Geosciences (2016).

22. Alpak, Faruk O and Riviere, Beatrice and Frank, Florian. A phase-field method for the direct simulation of two-phase flows in pore-scale media using a non-equilibrium wetting boundary condition. Computational Geosciences (2016).

23. Badalassi, Vittorio E and Ceniceros, Hector D and Banerjee, Sanjoy. Computation of multiphase systems with phase field models. Journal of computational physics (2003).

24. Blunt, Martin J. Flow in porous media—pore-network models and multiphase flow. Current opinion in colloid & interface science (2001).

25. Bandara, Uditha C and Tartakovsky, Alexandre M and Oostrom, Martinus and Palmer, Bruce J and Grate, Jay and Zhang, Changyong. Smoothed particle hydrodynamics pore-scale simulations of unstable immiscible flow in porous media. Advances in water resources (2013).

26. Jettestuen, Espen and Helland, Johan O and Prodanović. A level set method for simulating capillary-controlled displacements at the pore scale with nonzero contact angles. Water Resources Research (2013).

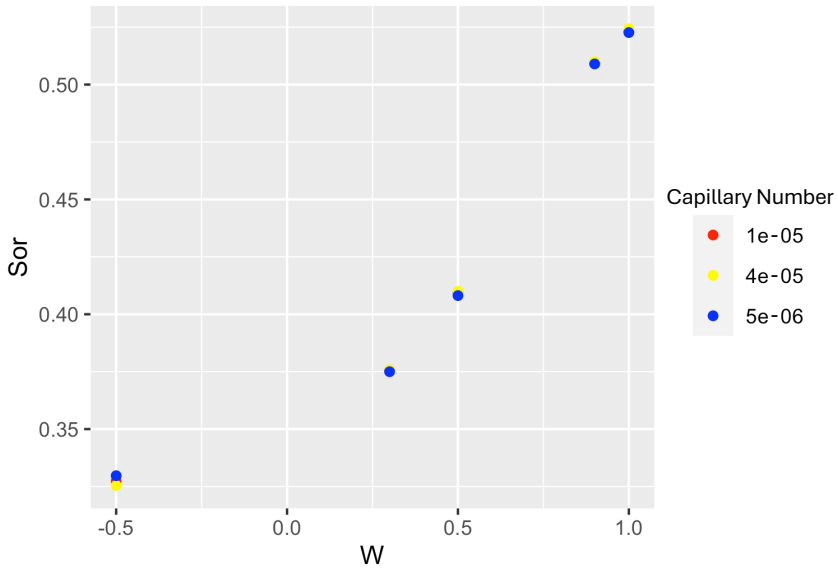

Figure 3. Residual oil saturation versus wettability W for the range of tested capillary numbers.

27. Wang, YD and Chung, Traiwit and Armstrong, Ryan T and McClure, J and Ramstad, Thomas and Mostaghimi, Peyman. Accelerated computation of relative permeability by coupled morphological and direct multiphase flow simulation. Journal of Computational Physics (2020).

28. Chung, Jaehong and Marcato, Agnese and Guiltinan, Eric J and Mukerji, Tapan and Viswanathan, Hari and Lin, Yen Ting and Santos, Javier E. Accelerating Multiphase Flow Simulations with Denoising Diffusion Model Driven Initializations. arXiv preprint arXiv:2406.19333 (2024).

29. Santos, Javier E and Xu, Duo and Jo, Honggeun and Landry, Christopher J and Prodanović. PoreFlow-Net: A 3D convolutional neural network to predict fluid flow through porous media. Advances in Water Resources (2020).

30. Latva-Kokko, M and Rothman, Daniel H. Scaling of dynamic contact angles in a lattice-Boltzmann model. Physical review letters (2007).

31. Payatakes, AC and Dias, Madalena M. Immiscible microdisplacement and ganglion dynamics in porous media. Reviews in Chemical Engineering (1984).

32. Garfi, Gaetano and John, Cé. Determination of the spatial distribution of wetting in the pore networks of rocks. Journal of Colloid and Interface Science (2022).

33. McClure, James E and Fan, Ming and Berg, Steffen and Armstrong, Ryan T and Berg, Carl Fredrik and Li, Zhe and Ramstad, Thomas. Relative permeability as a stationary process: Energy fluctuations in immiscible displacement. Physics of Fluids (2022).

34. Hansen, Alex and Flekkø. A statistical mechanics framework for immiscible and incompressible two-phase flow in porous media. Advances in Water Resources (2023).

35. Bedeaux, Dick and Kjelstrup, Signe. Fluctuation-dissipation theorems for multiphase flow in porous media. Entropy (2021).

36. Quintard, Michel and Whitaker, Stephen. Two-phase flow in heterogeneous porous media: The method of large-scale averaging. Transport in porous media (1988).

37. Wang, Ying Da and Meyer, Quentin and Tang, Kunning and McClure, James E and White, Robin T and Kelly, Stephen T and Crawford, Matthew M and Iacoviello, Francesco and Brett, Dan JL and Shearing, Paul R and others. Large-scale physically accurate modelling of real proton exchange membrane fuel cell with deep learning. Nature Communications (2023).

38. Rü". The Effect of Mixed Wettability on Pore Scale Flow Regimes Based on a Flooding Experiment in Ketton Limestone. Geophys. Res. Lett. (2019).

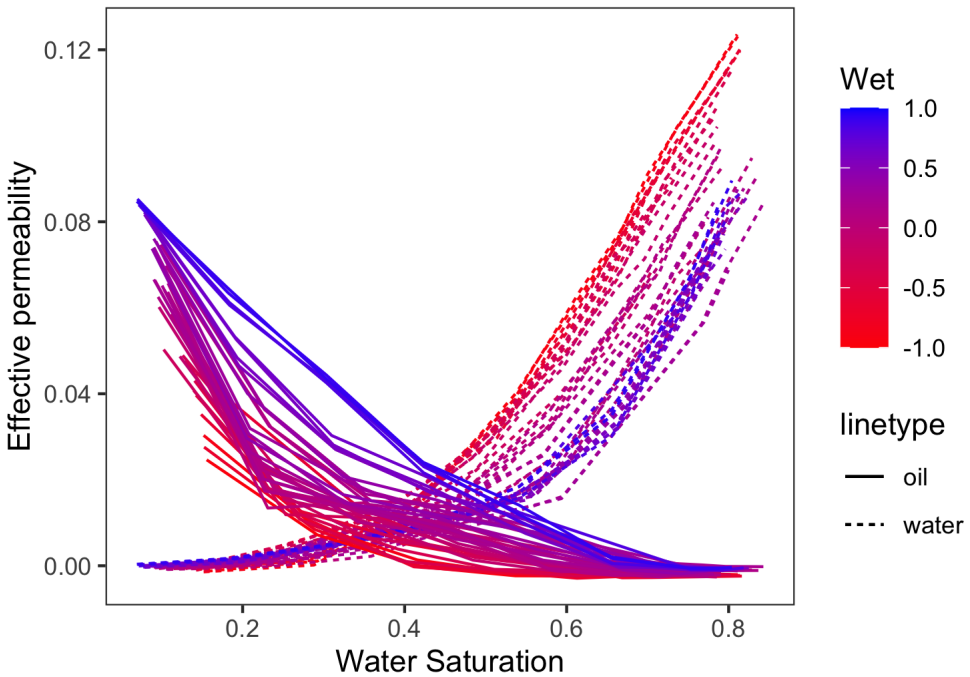

Figure 4. Relative permeability curves for all of the tested wetting distributions. All curves follow a bulk behaviour based on the wetting index (W).

39. Zhang, L. and Yao, J. and Zhao, J. and Li, A. and Sun, H. and Wan, Y. and Su, Y.. The influence of wettability and shut-in time on oil recovery through microscale simulation based on an ideal model. Journal of Natural Gas Science and Engineering (2017).

40. Jettestuen, E. and Aursjø. Workflow for Direct Pore-Scale Simulation of Relative Permeability and Capillary Pressure Curves with Hysteresis at Low Capillary Numbers. (2024).

41. Wyckoff, RD and Botset, HG. The flow of gas-liquid mixtures through unconsolidated sands. physics (1936).

42. Lin, Qingyang and Bijeljic, Branko and Berg, Steffen and Pini, Ronny and Blunt, Martin J and Krevor, Samuel. Minimal surfaces in porous media: Pore-scale imaging of multiphase flow in an altered-wettability Bentheimer sandstone. Physical Review E (2019).

43. Fredrich, Joanne T and Lakshtanov, DL and Lane, NM and Liu, Elizabeth B and Natarajan, CS and Ni, Dianne M and Toms, JJ. Digital rocks: Developing an emerging technology through to a proven capability deployed in the business. (2014).

44. McClure, James E and Wang, Hao and Prins, Jan F and Miller, Cass T and Feng, Wu-chun. Petascale application of a coupled CPU-GPU algorithm for simulation and analysis of multiphase flow solutions in porous medium systems. (2014).

45. Andrä. Digital rock physics benchmarks—Part II: Computing effective properties. Computers & Geosciences (2013).

46. Reynolds, Catriona A and Menke, Hannah and Andrew, Matthew and Blunt, Martin J and Krevor, Samuel. Dynamic fluid connectivity during steady-state multiphase flow in a sandstone. Proceedings of the National Academy of Sciences (2017).

47. Sripal, Edison and James, LA. Application of an optimization method for the restoration of core samples for SCAL experiments. Petrophysics (2018).

48. Schlü. Image processing of multiphase images obtained via X-ray microtomography: a review. Water Resources Research (2014).

49. Berg, Steffen and Ott, Holger and Klapp, Stephan A and Schwing, Alex and Neiteler, Rob and Brussee, Niels and Makurat, Axel and Leu, Leon and Enzmann, Frieder and Schwarz, Jens-Oliver and others. Real-time 3D imaging of Haines jumps in porous media flow. Proceedings of the National Academy of Sciences (2013).

50. Ramstad, Thomas. Bentheimer micro-CT with waterflood. (2025).

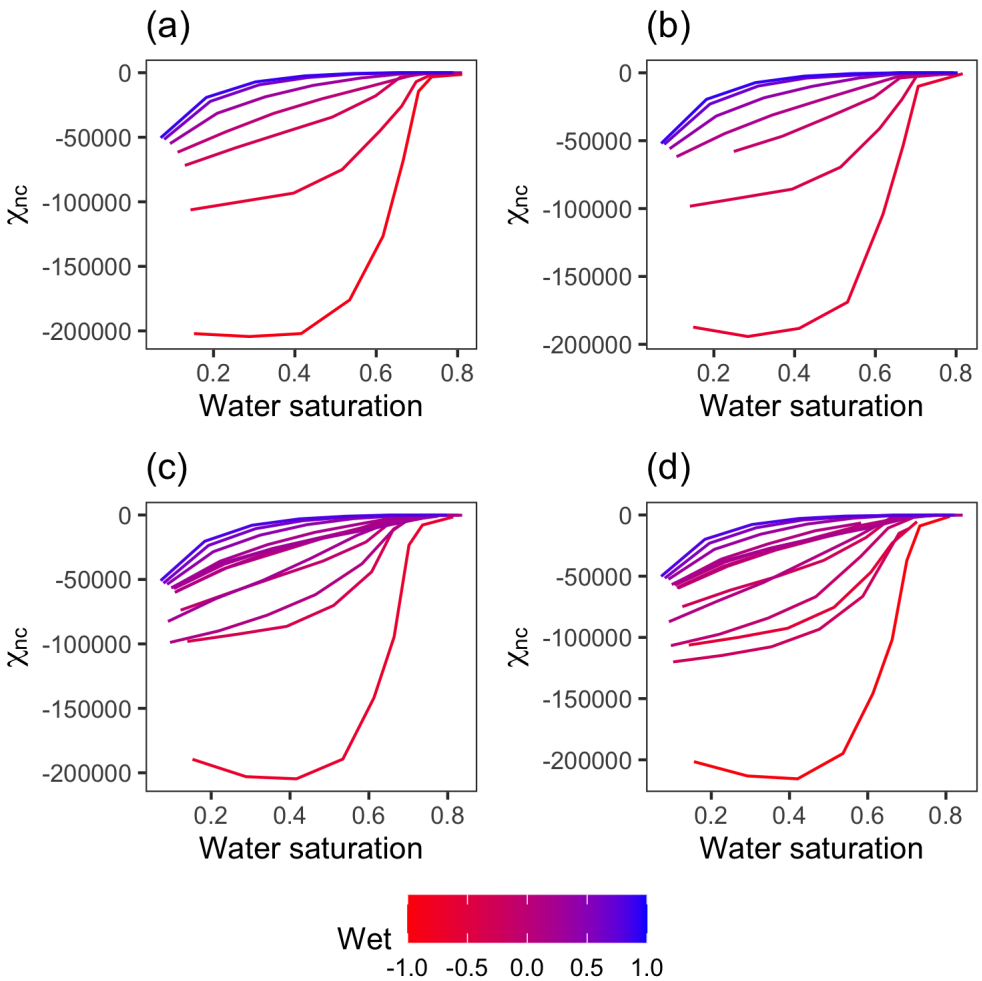

Figure 5. Euler characteristic for the connected NWP follows similar trends regardless of the distributed wetting conditions; homogeneous (a), mixed (b), fractional (c), hybrid (d).

51. Armstrong, Ryan and Rücker, Maja and Berg, Steffen and McClure, James. Fractional Flow Experiments. (2025).

52. Armstrong, Ryan and Mostaghimi, Peyman and McClure, James. Multimineral Model. (2025).

53. Li, Zhe and McClure, James and Ramstad, Thomas. Bentheimer Sandstone Two-Fluid Flow Simulation Resembling Special Core Analysis Protocol. (2025).

54. Gray, William G and Miller, Cass T. Introduction to the thermodynamically constrained averaging theory for porous medium systems. (2014).

55. Armstrong, Ryan. LBPM Simulations. https://doi.org/10.5281/zenodo.13836046 ().

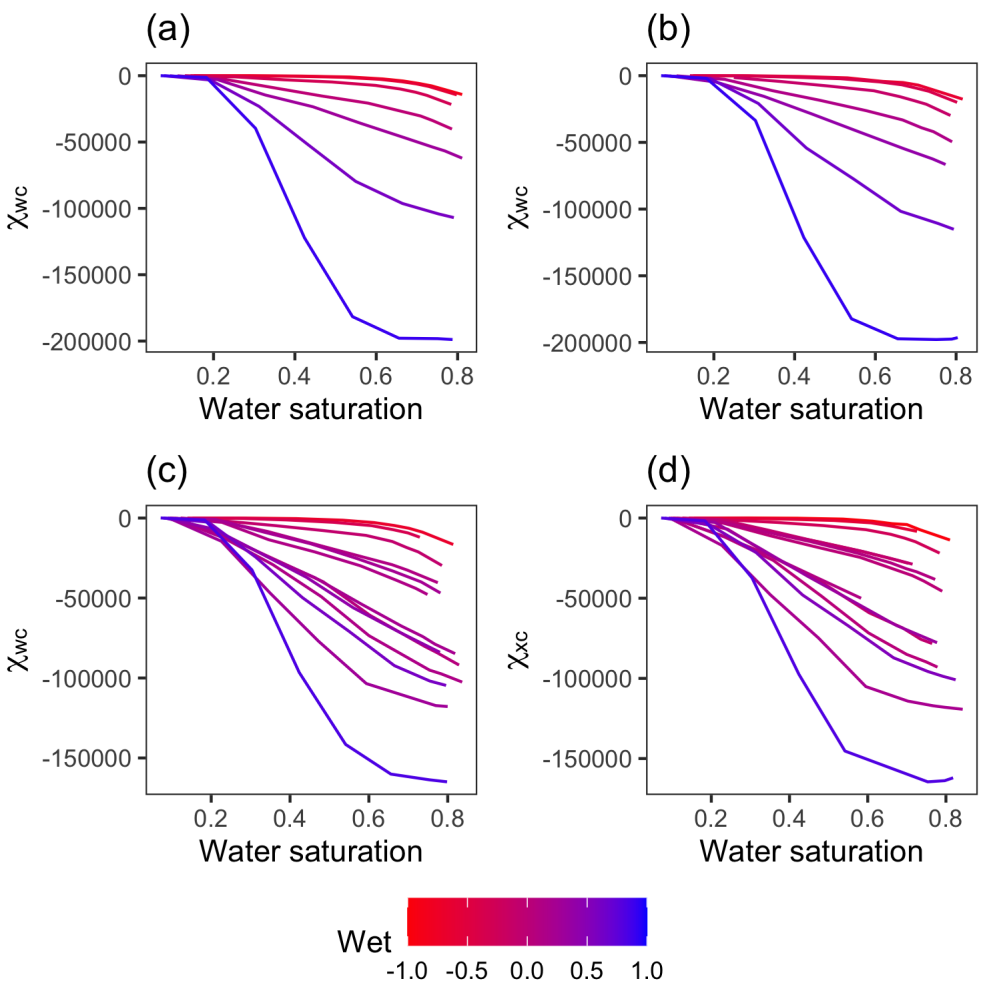

Figure 6. Euler characteristic for the connected WP follows similar trends regardless of the distributed wetting conditions; homogeneous (a), mixed (b), fractional (c), hybrid (d).

Quantities	Description
time	Timestep
rn	Density for phase n (input parameter)
rw	Density for phase w (input parameter)
nun	Kinematic viscosity for phase n (input parameter)
nuw	Kinematic viscosity for phase w (input parameter)
Fx	External force in x direction (input parameter)
Fy	External force in y direction (input parameter)
Fz	External force in z direction (input parameter)
iftwn	Interfacial tension (input parameter)
wet	Total solid wetting energy
pwc	Average pressure for connected part of phase w
pwd	Average pressure for disconnected part of phase w
pnc	Average pressure for connected part of phase n
pnd	Average pressure for disconnected part of phase n
Mwc	Mass for connected part of phase w
Mwd	Mass for disconnected part of phase w
Mwi	Mass for phase within diffuse interface region
Mnc	Mass for connected part of phase n
Mnd	Mass for disconnected part of phase n
Mni	Mass for phase n within diffuse interface region
Msw	Mass for component w within 2 voxels of solid
Msn	Mass for component n within 2 voxels of solid
Pwc_x	x-momentum for connected part of phase w
Pwd_x	x-momentum for disconnected part of phase w
Pwi_x	x-momentum for phase w within diffuse interface
Pnc_x	x-momentum for connected part of phase n
Pnd_x	x-momentum for disconnected part of phase n
Pni_x	x-momentum for phase n within diffuse interface
Psw_x	x-momentum for phase w within 2 voxels of solid
Psn_x	x-momentum for phase n within 2 voxels of solid
Pwc_y	y-momentum for connected part of phase w
Pwd_y	y-momentum for disconnected part of phase w
Pwi_y	y-momentum for phase w within diffuse interface
Pnc_y	y-momentum for connected part of phase n
Pnd_y	y-momentum for disconnected part of phase n
Pni_y	y-momentum for phase n within diffuse interface
Psw_y	y-momentum for phase w within 2 voxels of solid
Psn_y	y-momentum for phase n within 2 voxels of solid
Pwc_z	z-momentum for connected part of phase w
Pwd_z	z-momentum for disconnected part of phase w
Pwi_z	z-momentum for phase w within diffuse interface
Pnc_z	z-momentum for connected part of phase n
Pnd_z	z-momentum for disconnected part of phase n
Pni_z	z-momentum for phase n within diffuse interface
Psw_z	z-momentum for phase w within 2 voxels of solid
Psn_z	z-momentum for phase n within 2 voxels of solid

Table 3. Measured quantities and their descriptions within sub-phase analysis (Part 1).

Quantities	Description
Kwc	Kinetic energy for transport within connected part of phase w
Kwd	Kinetic energy for transport within disconnected part of phase w
Kwi	Kinetic energy for transport of phase w within diffuse interface region
Knc	Kinetic energy for transport in connected part of phase n
Knd	Kinetic energy for transport within disconnected part of phase n
Kni	Kinetic energy for transport of phase n within diffuse interface region
Dwc	Viscous dissipation for connected pathway for phase w
Dwd	Viscous dissipation for disconnected part of phase w
Dnc	Viscous dissipation for connected pathway for phase n
Dnd	Viscous dissipation for disconnected part of phase n
Vwc	Volume for connected pathway for phase w
Awc	Surface area for connected pathway for phase w
Hwc	Integral mean curvature for connected pathway for phase w
Xwc	Euler characteristic for connected pathway for phase w
Vwd	Volume for disconnected phase w
Awd	Surface area for disconnected phase w
Hwd	Integral mean curvature for disconnected phase w
Xwd	Euler characteristic for disconnected phase w
Nwd	Number of connected components in disconnected phase w
Vnc	Volume for connected pathway for phase n
Anc	Surface area for connected pathway for phase n
Hnc	Integral mean curvature for connected pathway for phase n
Xnc	Euler characteristic for connected pathway for phase n
Vnd	Volume for disconnected phase n
And	Surface area for disconnected phase n
Hnd	Integral mean curvature for disconnected phase n
Xnd	Euler characteristic for disconnected phase n
Nnd	Number of connected components within disconnected phase n
Vi	Volume for diffuse interface region
Ai	Surface area for boundary of diffuse interface region
Hi	Integral mean curvature for boundary of diffuse interface region
Xi	Euler characteristic for diffuse interface region
Vic	Volume for connected interface region
Aic	Surface area for boundary of connected interface region
Hic	Integral mean curvature for connected interface region
Xic	Euler characteristic for connected interface region
Nic	Number of connected components in connected interface region

Table 4. Measured quantities and their descriptions within sub-phase analysis (Part 2).

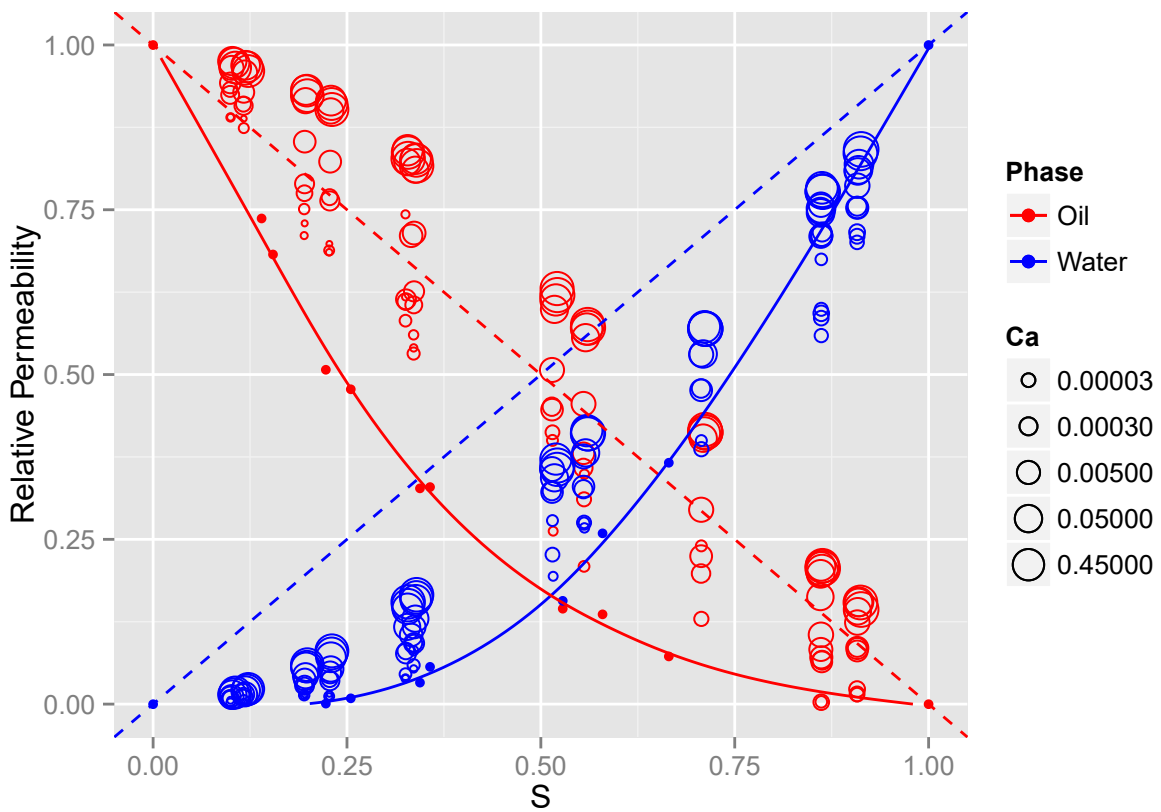

Figure 7. Relative permeability data for Robuglass. The data ranges over various capillary numbers and the solid lines correspond to connected phase permeability only.

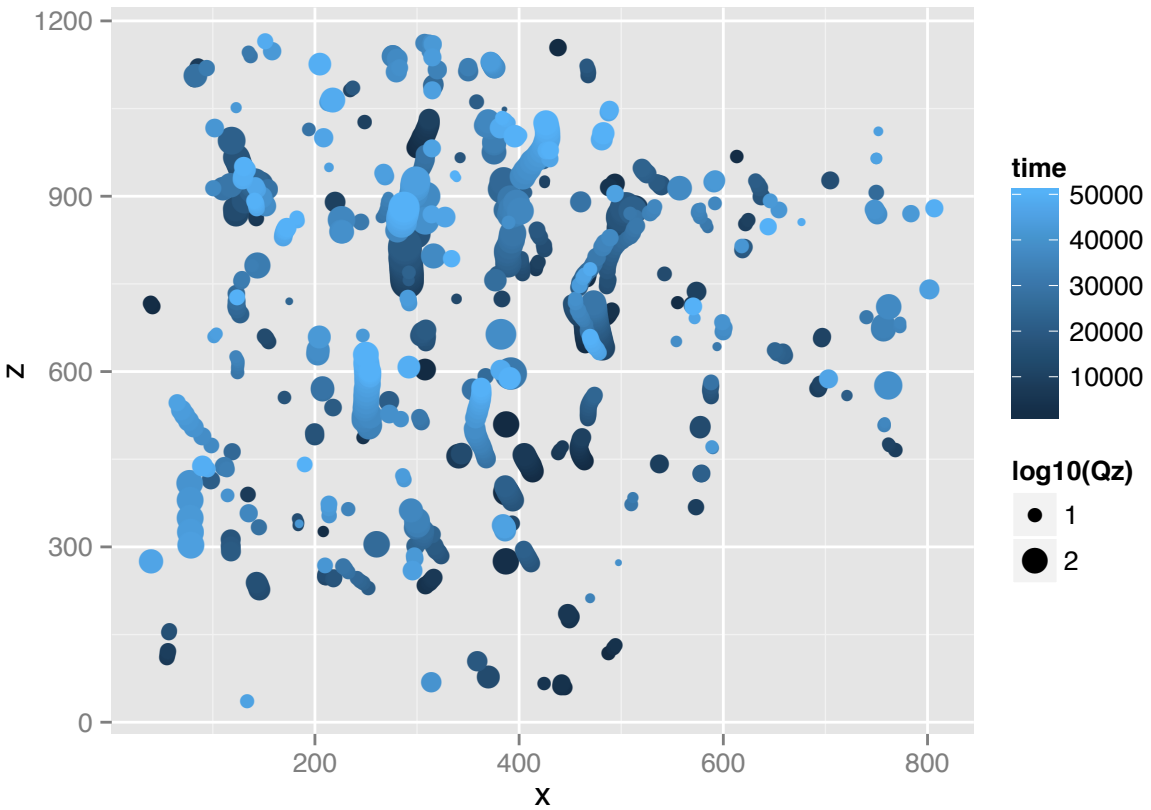

Figure 8. NWP ganglion trajectories in the Z-Y plane.

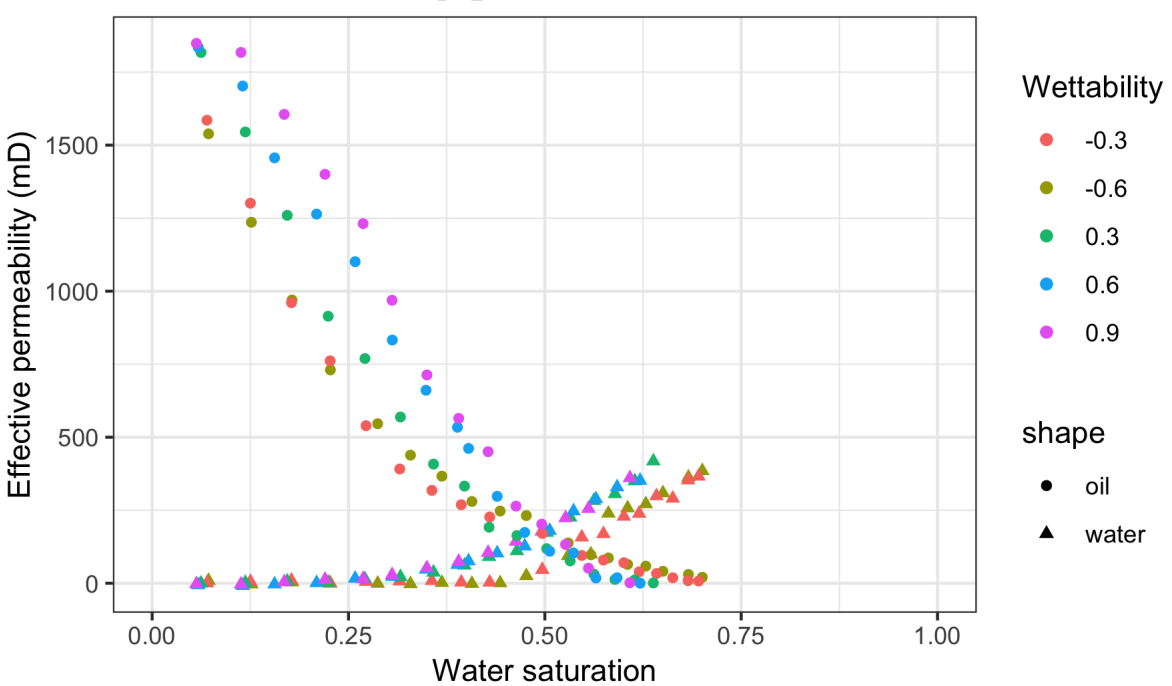

Figure 9. Relative permeability curves for all of the tested wetting conditions. All curves follow a bulk behaviour based on the wetting index (W).

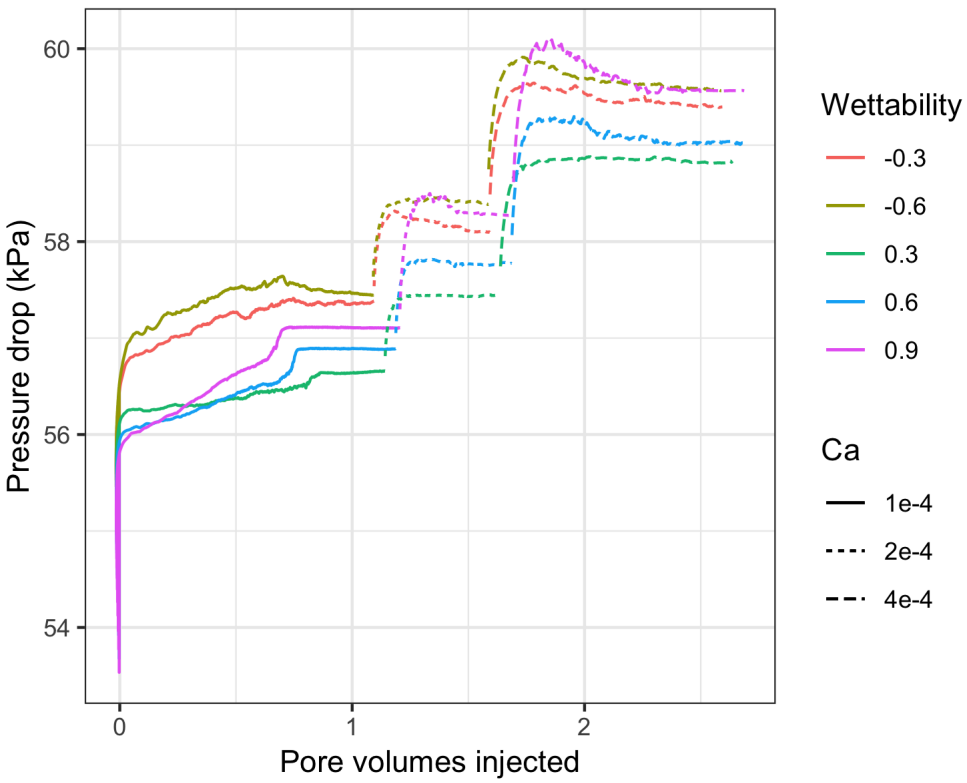

Figure 10. Imbibition mode core flooding data for all of the tested wetting conditions.

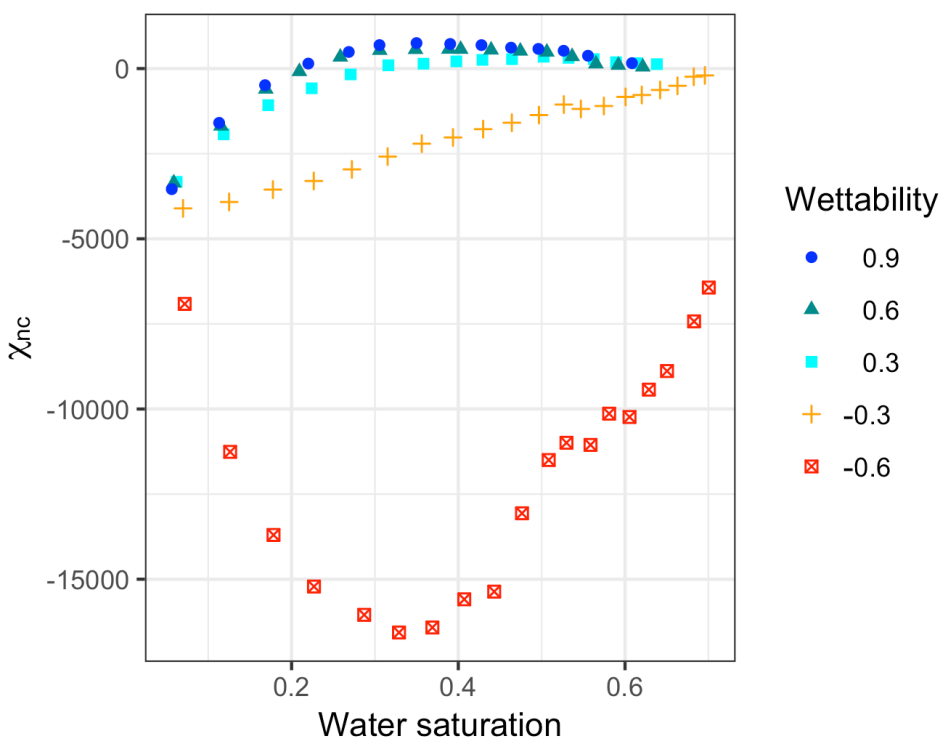

Figure 11. Euler characteristic of the NWP versus saturation for different wetting conditions

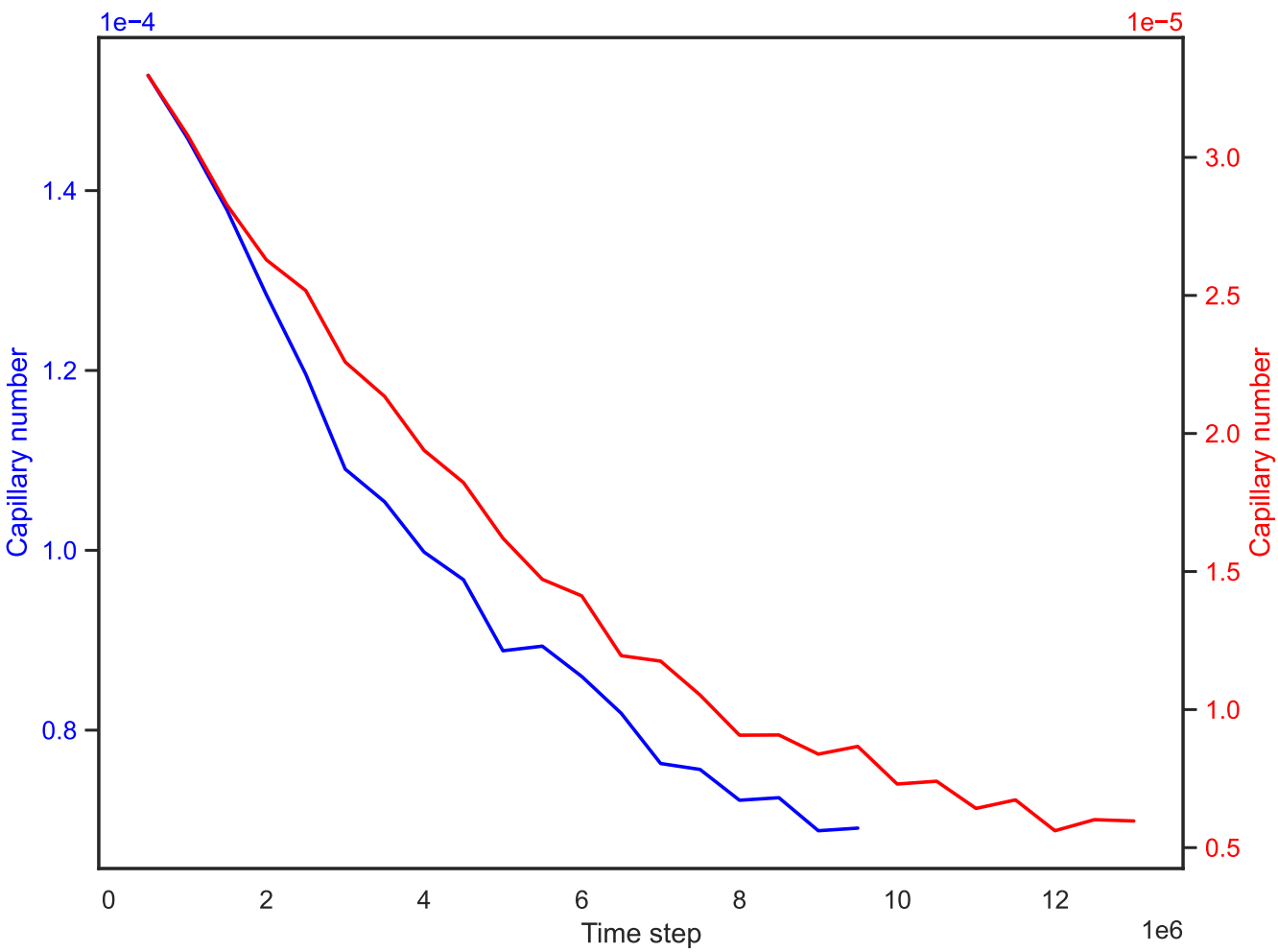
1e−4
1e−5
1.4
1.2
1.0
0.8
3.0
2.5
2.0
1.5
1.0
0.5
Capillary number
Capillary number
0
2
4
6
8
10
12
Time step
1e6

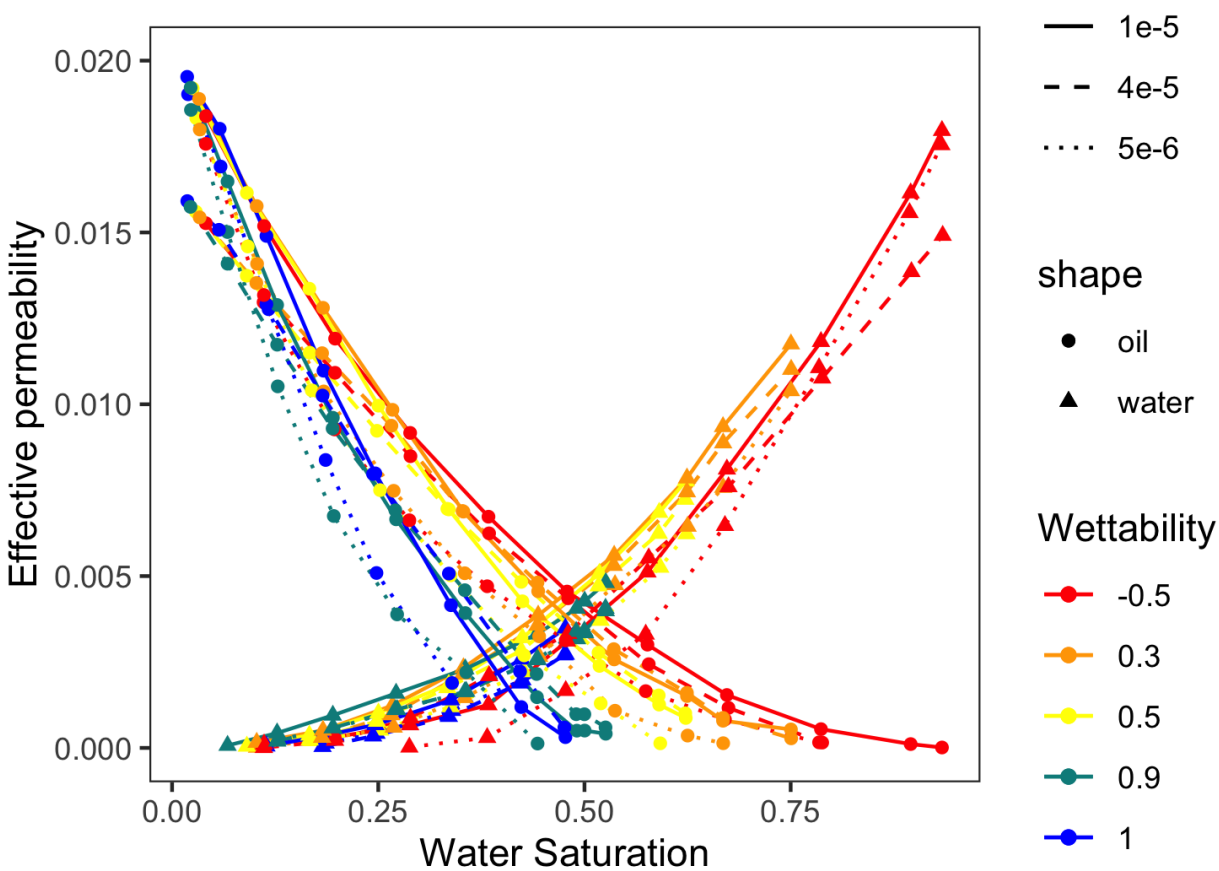
Effective permeability
0.020
0.015
0.010
0.005
0.000
0.00
0.25
0.50
0.75
Water Saturation
1e-5
4e-5
5e-6
shape
oil
water
Wettability
-0.5
0.3
0.5
0.9
1

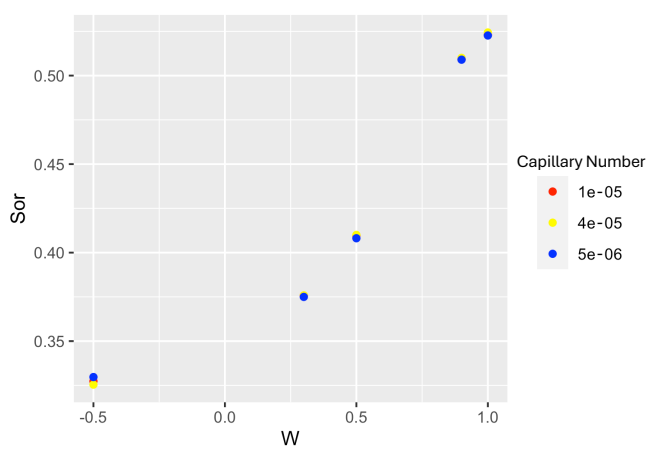
0.50
0.45
0.40
0.35
Sor
-0.5
0.0
0.5
1.0
W
Capillary Number
1e-05
4e-05
5e-06

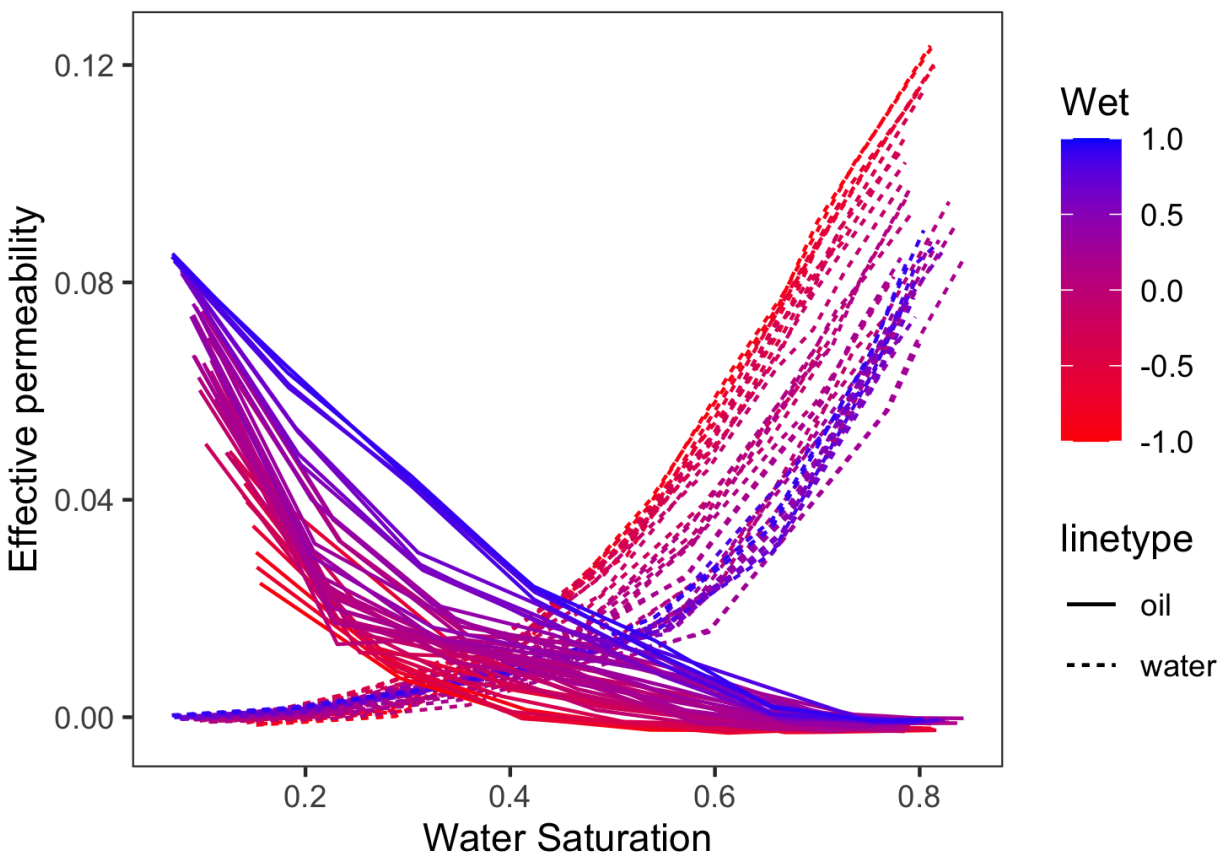
0.12
0.08
0.04
0.00
Effective permeability
0.2
0.4
0.6
0.8
Water Saturation
Wet
1.0
0.5
0.0
-0.5
-1.0
linetype
oil
water

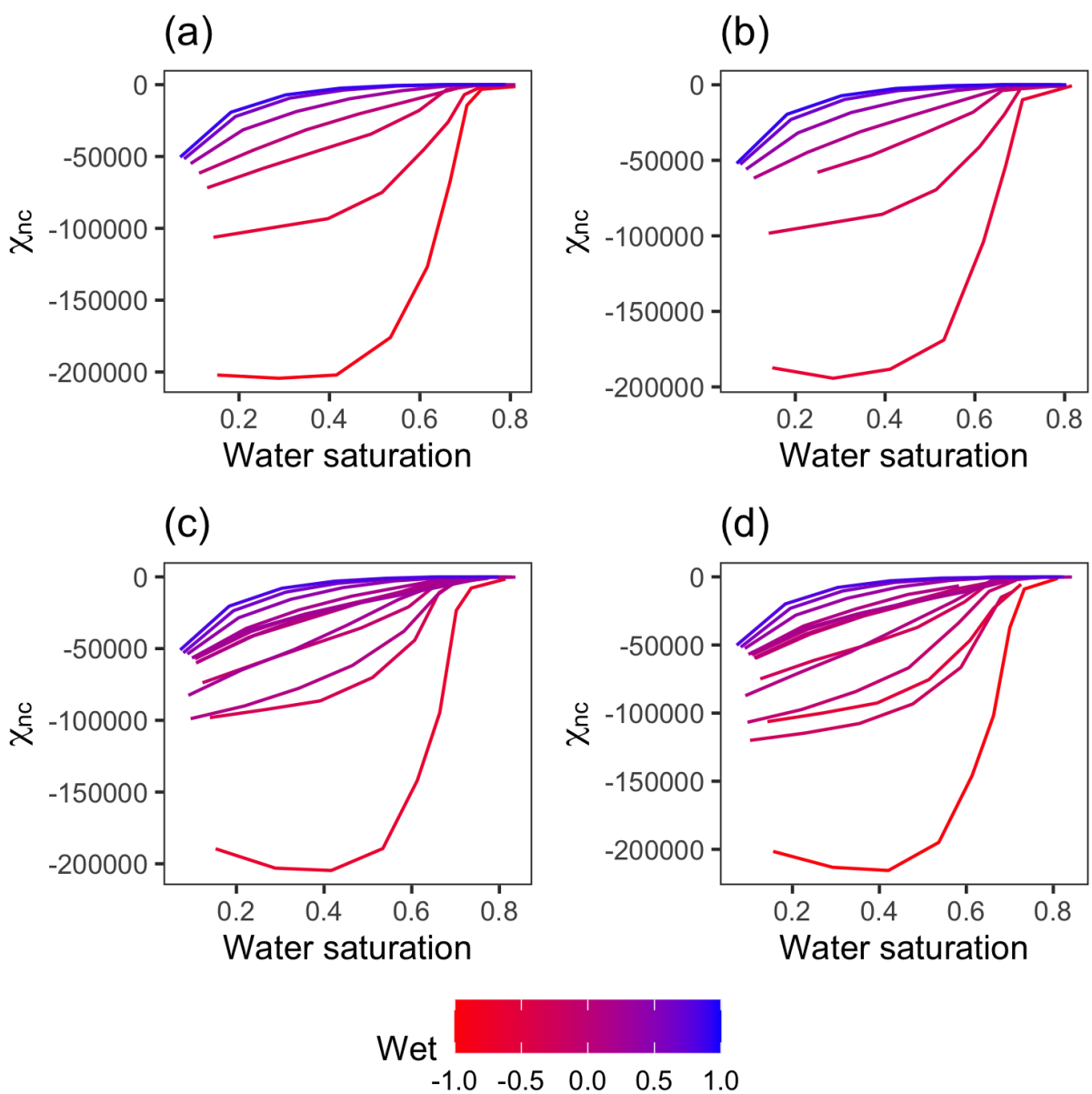
(a)
(b)
(c)
(d)
χnc
0
-50000
-100000
-150000
-200000
0.2
0.4
0.6
0.8
Water saturation
Wet
-1.0
-0.5
0.0
0.5
1.0

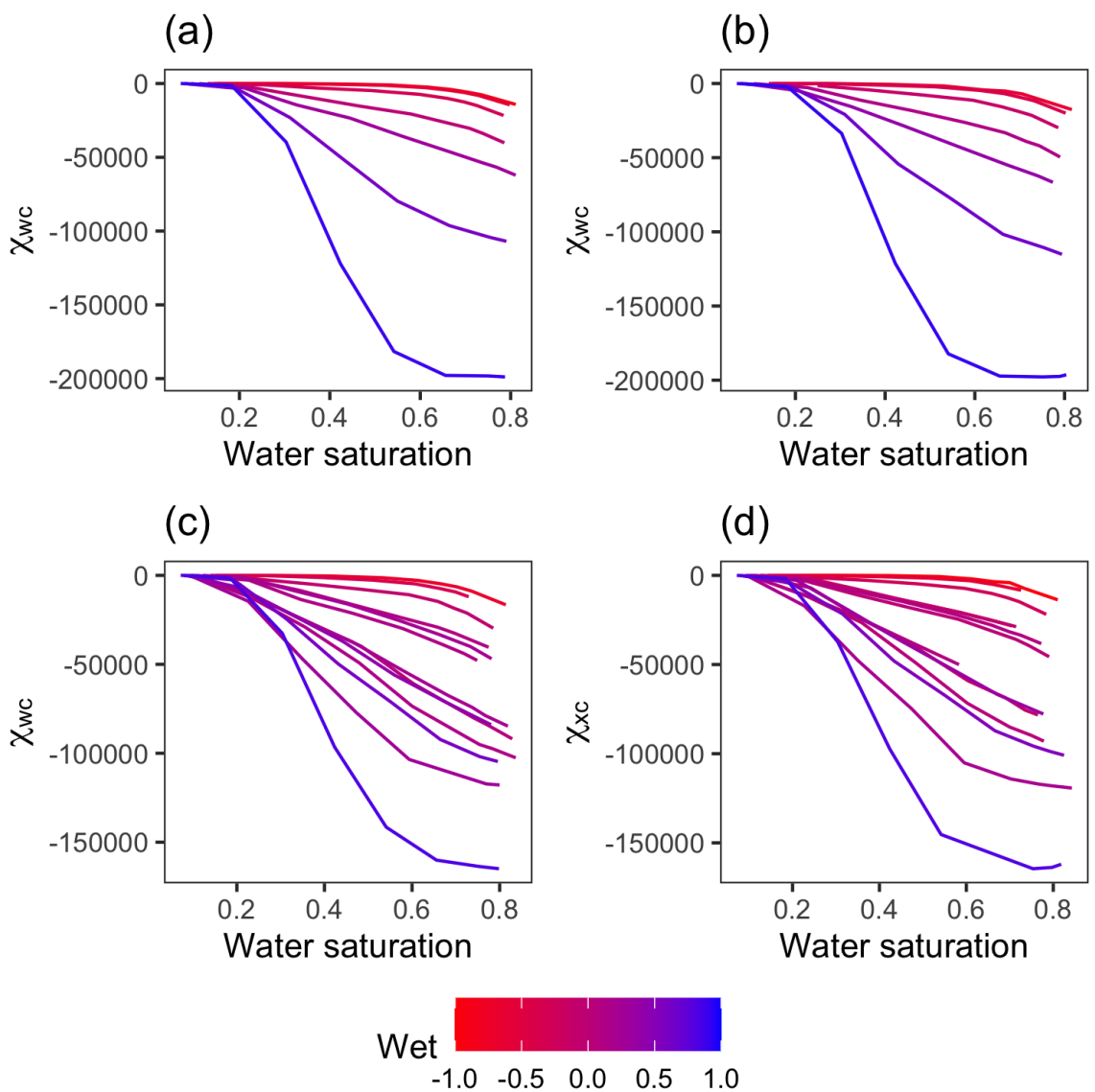
(a)
(b)
(c)
(d)
0
-50000
-100000
-150000
-200000
χ_{wc}
χ_{xc}
0.2
0.4
0.6
0.8
Water saturation
Wet
-1.0
-0.5
0.0
0.5
1.0

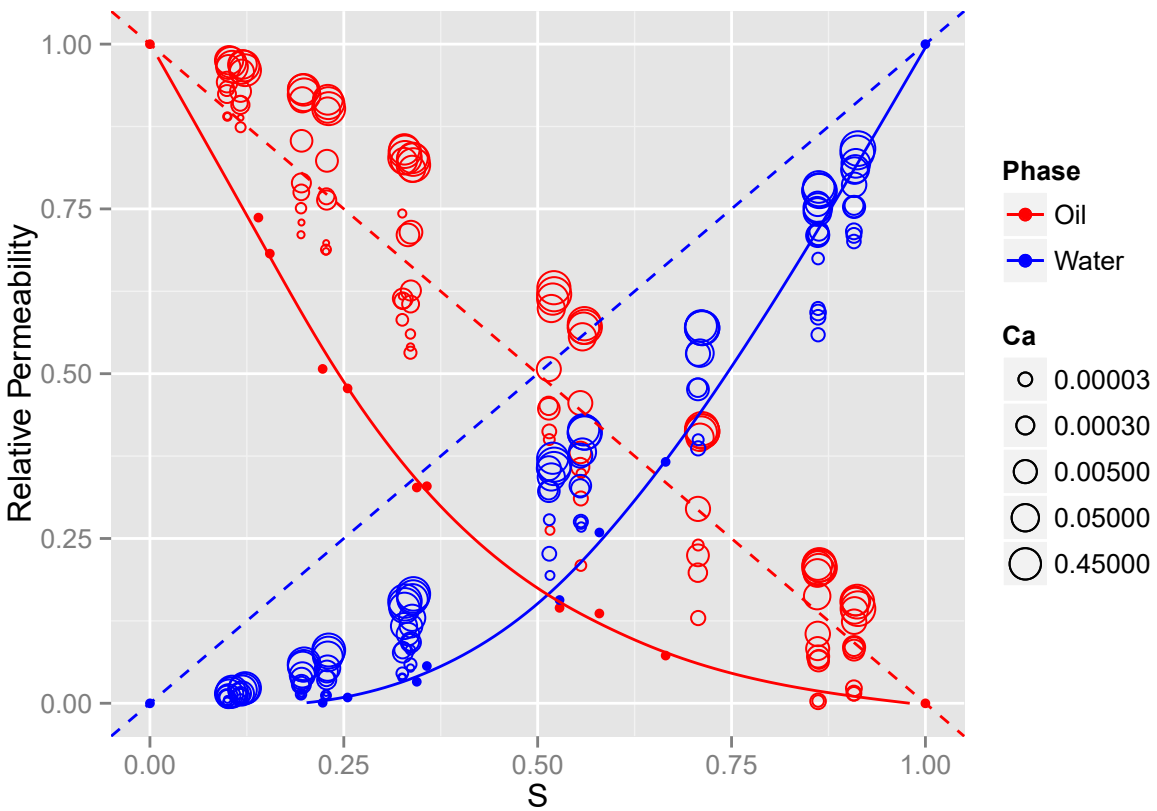
Relative Permeability
1.00
0.75
0.50
0.25
0.00
0.00
0.25
0.50
0.75
1.00
S
Phase
Oil
Water
Ca
0.00003
0.00030
0.00500
0.05000
0.45000

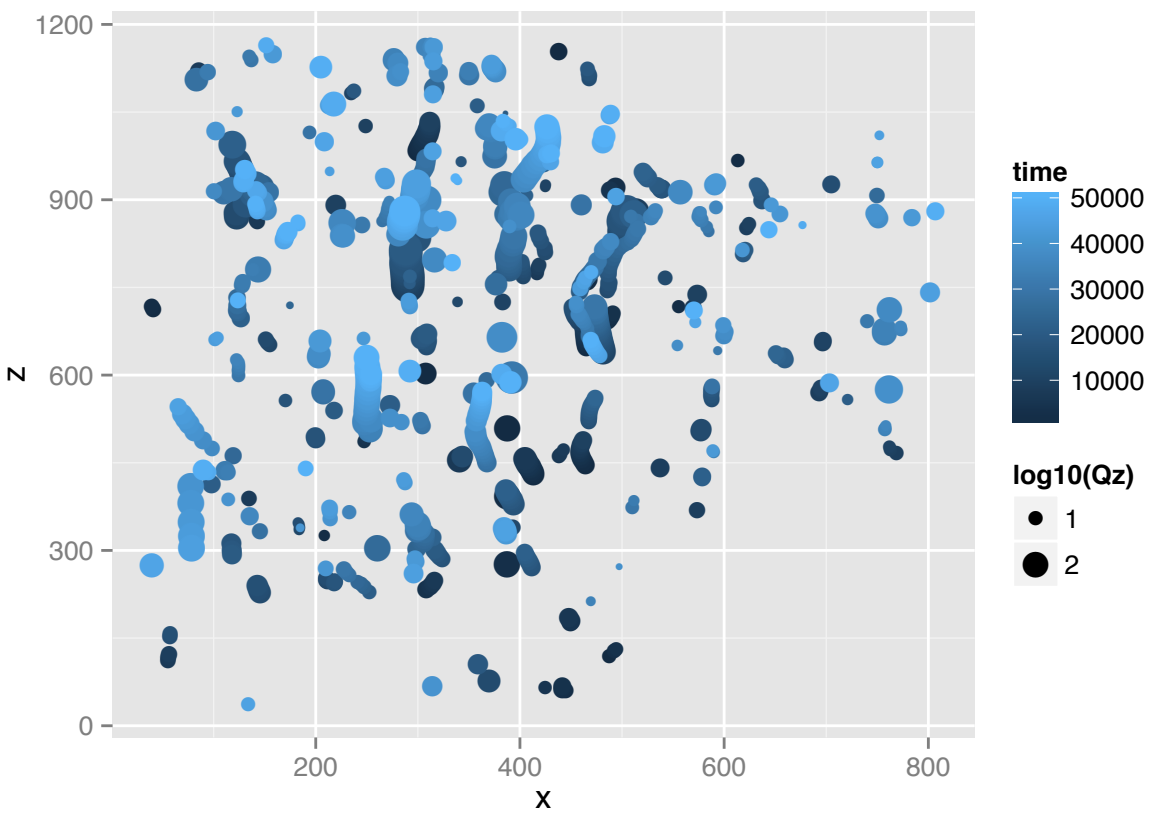
1200
900
600
300
0
z
200
400
600
800
x
time
50000
40000
30000
20000
10000
log10(Qz)
1
2

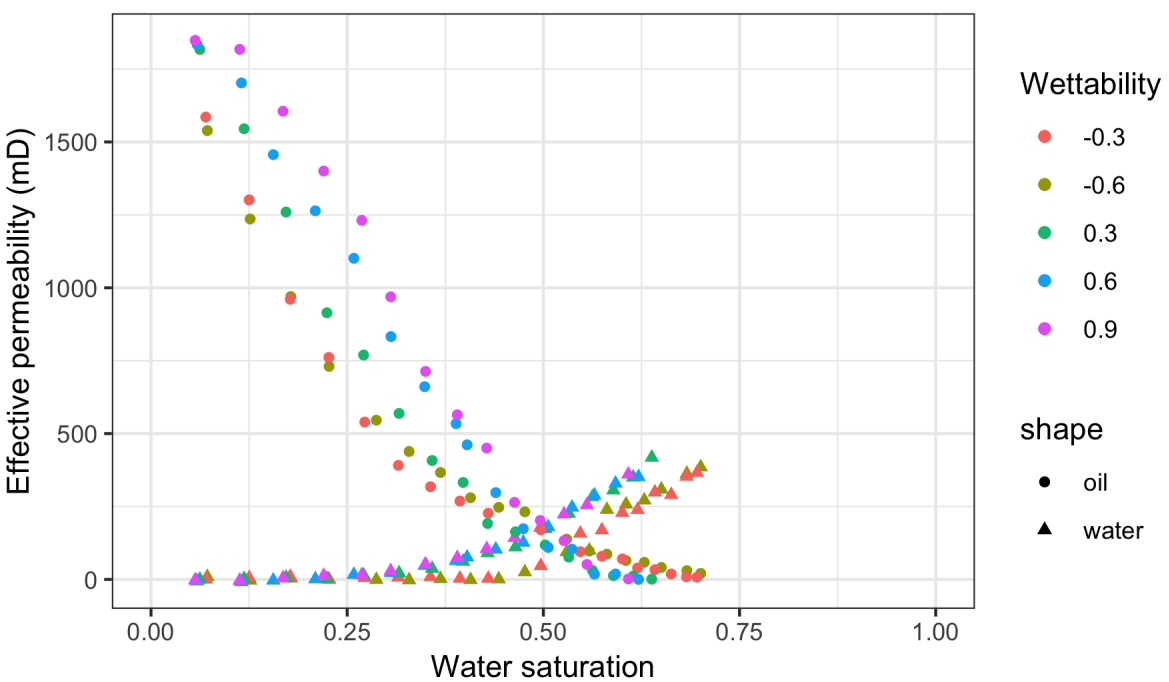
Effective permeability (mD)
1500
1000
500
0
0.00
0.25
0.50
0.75
1.00
Water saturation
Wettability
-0.3
-0.6
0.3
0.6
0.9
shape
oil
water

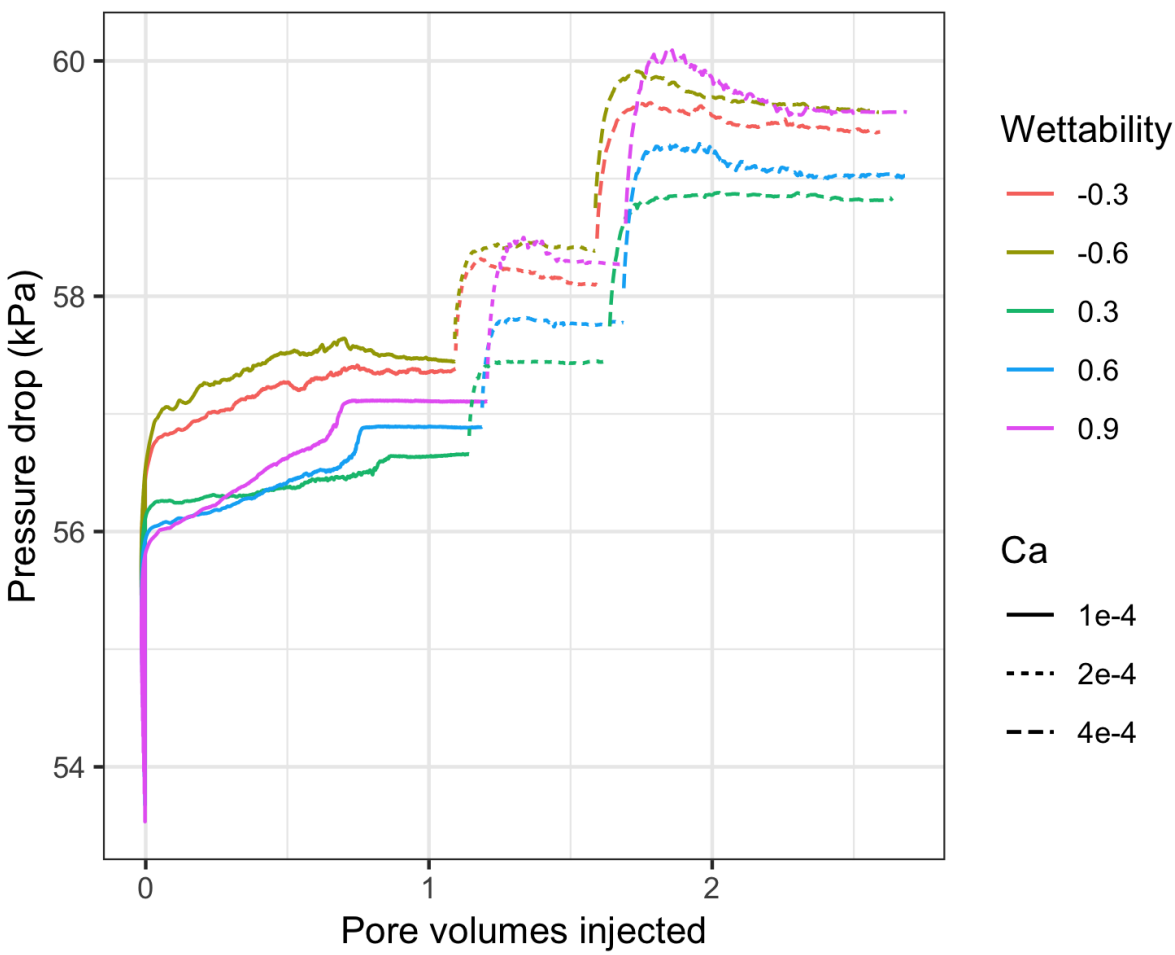
Pressure drop (kPa)
60
58
56
54
0
1
2
Pore volumes injected
Wettability
-0.3
-0.6
0.3
0.6
0.9
Ca
1e-4
2e-4
4e-4

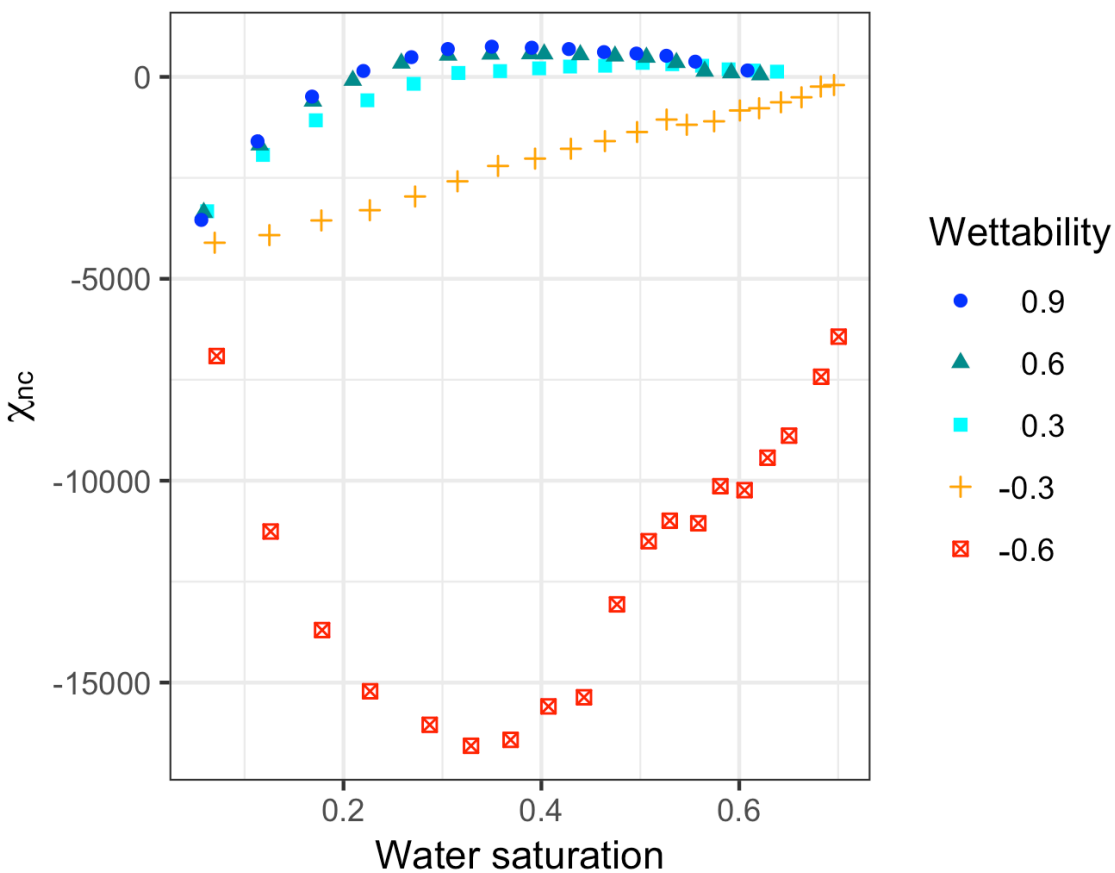
0
-5000
-10000
-15000
χnc
0.2
0.4
0.6
Water saturation
Wettability
0.9
0.6
0.3
-0.3
-0.6